JGR Solid Earth

RESEARCH ARTICLE
10.1029/2023JB026839

Scaling Microseismic Cloud Shape During Hydraulic Stimulation Using In Situ Stress and Permeability

Y. Mukuhira[1], M. Yang[1,2], T. Ishibashi[3], K. Okamoto[3], H. Moriya[4], Y. Kumano[5], H. Asanuma[3], S. A. Shapiro[6], J. L. Rubinstein[7], T. Ito[1], K. Yan[1,2], and Y. Zuo[2]

[1]Institute of Fluid Science, Tohoku University, Sendai, Japan, [2]State Key Laboratory of Oil and Gas Reservoir Geology and Exploitation, Chengdu University of Technology, Chengdu, China, [3]Fukushima Renewable Energy Institute, National Institute of Advanced Industrial Science and Technology, Koriyama, Japan, [4]School of Engineering, Tohoku University, Sendai, Japan, [5]JAPEX Co., Ltd, Tokyo, Japan, [6]Freie Universität Berlin, Berlin, Germany, [7]United States Geological Survey, Menlo Park, CA, USA

Abstract Forecasting microseismic cloud shape as a proxy of stimulated rock volume may improve the design of an energy extraction system. The microseismic cloud created during hydraulic stimulation of geothermal reservoirs is known empirically to extend in the general direction of the maximum principal stress. However, this empirical relationship is often inconsistent with reported results, and the cloud growth process remains poorly understood. This study investigates microseismic cloud growth using data obtained from a hydraulic stimulation project in Basel, Switzerland, and explores its correlation with measured in situ stress. We applied principal component analysis to a time series of microseismicity for macroscopic characterization of microseismic cloud growth in two- and three-dimensional space. The microseismic cloud, in addition to extending in the general direction of maximum principal stress, expanded in the direction of intermediate principal stress. The orientation of the least microseismic cloud growth was stable and almost identical to the minimum principal stress direction. Further, microseismic cloud shape ratios showed good agreement when compared with in situ stress magnitude ratios. The permeability tensor estimated from microseismicity also provided a good correlation in terms of direction and magnitude with the microseismic cloud growth. We show that in situ stress plays a dominant role by controlling the permeability of each existing fracture in the reservoir fracture system. Consequently, microseismic cloud growth can be scaled by in situ stress as a first-order approximation if there is sufficient variation in the orientation of existing faults.

Plain Language Summary In the next generation of geothermal development, massive volumes of fluid are injected underground to either create a potential geothermal reservoir or enhance fluid flow. In that process, water migration can be tracked by small earthquakes that are rarely felt by humans. The region of small earthquakes can be regarded as an active geothermal reservoir. Knowing the reservoir's shape may improve the assessment and design of the energy extraction system. However, it is difficult to forecast the shape of a possible geothermal reservoir prior to fluid injection. This study investigated the temporal variations in the shape of the region of small earthquakes caused by fluid injection using the data from the geothermal project at Basel, Switzerland. We found that the region's shape is correlated to the local stress when the reservoir hosted various existing fractures. Thus, the geothermal reservoir shape can be forecasted in advance using knowledge of the regional stress, which may allow for better assessment of geothermal development.

Key Points:

- Microseismic cloud shape is correlated to in situ stress ratio and the permeability tensor
- Microseismic cloud growth is mainly controlled by in situ stress if there is sufficient variation in existing fracture orientation
- Microseismic cloud shape can be forecasted macroscopically with the in situ stress ratio, for use in designing an energy extraction system

Supporting Information:

Supporting Information may be found in the online version of this article.

Correspondence to:

Y. Mukuhira,
mukuhira@tohoku.ac.jp

Citation:

Mukuhira, Y., Yang, M., Ishibashi, T., Okamoto, K., Moriya, H., Kumano, Y., et al. (2023). Scaling microseismic cloud shape during hydraulic stimulation using in situ stress and permeability. *Journal of Geophysical Research: Solid Earth*, *128*, e2023JB026839. https://doi.org/10.1029/2023JB026839

Received 14 APR 2023
Accepted 23 JUL 2023

Author Contributions:

Conceptualization: Y. Mukuhira, S. A. Shapiro
Data curation: Y. Mukuhira, T. Ishibashi, K. Okamoto, H. Moriya, Y. Kumano, H. Asanuma
Formal analysis: Y. Mukuhira
Funding acquisition: Y. Mukuhira, H. Asanuma, Y. Zuo
Investigation: Y. Mukuhira, M. Yang, K. Yan
Methodology: Y. Mukuhira
Project Administration: H. Asanuma
Resources: Y. Mukuhira

1. Introduction

A stable energy supply supports broad economic and social activities. Additionally, the transition from hydrocarbon resources associated with carbon dioxide (CO_2) emissions to renewable energy may mitigate global warming and its various associated risks. Geothermal energy is one of the most promising renewable energy sources, as it is suitable for meeting energy baseload demands. Several attempts have been made to increase geothermal energy use even in non-volcanic regions (Evans et al., 2012) through the development of an enhanced geothermal system (EGS). In EGS development, geothermal energy is extracted from a greater depth than that would be utilized in volcanic regions in order to access high-temperature geothermal resources and generate energy more economically. Based on the permeability and the presence of fluid in the target formation, an engineering operation is typically employed to either increase the permeability or to inject fluid as a heat exchange medium. In many cases of EGS, fluid injection is undertaken as a means of hydraulic stimulation to improve the permeability through

Software: Y. Mukuhira
Supervision: H. Moriya, Y. Kumano, H. Asanuma, S. A. Shapiro, J. L. Rubinstein, T. Ito, Y. Zuo
Validation: Y. Mukuhira, S. A. Shapiro, J. L. Rubinstein, T. Ito
Visualization: Y. Mukuhira, K. Yan
Writing – original draft: Y. Mukuhira, T. Ishibashi, H. Moriya, Y. Kumano
Writing – review & editing: Y. Mukuhira

hydro-shearing of existing fractures. Naturally, a potential EGS reservoir, which often consists of granite, hosts several existing fractures; thus, boreholes often intersect with these existing fractures. In this case, fluid can be injected at a lower wellhead pressure than the minimum principal stress (σ_3). The injected water migrates via the existing fracture system in the reservoir, and increased pore pressure concurrently or static stress change due to preceding shear slip, thermal effect, or poroelastic effect destabilizes the existing faults. When friction decreases enough to be overcome by shear stress or formation stresses are sufficiently altered, shear slip occurs on the existing fractures (Pine & Batchelor, 1984; Zoback, 2007), resulting in microseismicity. The magnitude of such microseismicity is typically smaller than 2, but in some cases earthquakes larger than magnitude 2 have occurred (Ellsworth, 2013; Evans et al., 2012; Kim et al., 2018; Majer et al., 2007). This is the main process of EGS engineering reservoir development, as shear slip on existing fractures enhances the reservoir permeability (e.g., Watanabe et al., 2008; Yeo et al., 1998).

Measurement and analysis of microseismicity are essential parts of EGS, involving the monitoring of hydraulic stimulation and visualization of the shape and geometry of the artificial reservoirs. Microseismic data are automatically processed, and the hypocenter and magnitude of microseismicity are determined (e.g., Dyer et al., 2008; Gharti et al., 2010; Grigoli et al., 2016). Due to uncertainty in the phase arrival and velocity model, microseismic hypocenters often show a cloud shape, that is, the microseismic cloud (hereafter, the MS cloud), regardless of the magnitude. Post analysis by experts includes refined phase picking, relocation of the hypocenter, estimation of the source parameters such as moment magnitude, stress drop, and focal mechanism (e.g., Fehler et al., 2001). Relocated hypocenters often delineate a much sharper image of the existing fracture system than the automatically determined MS cloud. Therefore, well-determined MS cloud information can be used as a proxy for stimulated rock volume and can be used to indicate the location of production wells, as well as to identify the fracture system for heat exchange and aid in reservoir management (e.g., Dyer et al., 2008; Evans, 2005; Majer et al., 2007).

Many have shown that the MS cloud typically grows in the direction of maximum principal stress (σ_1) (e.g., Fehler, 1989; Fehler et al., 1987; Häring et al., 2008; Roff et al., 1996; Tezuka & Niitsuma, 2000). The conceptual fracture model for earthquake swarms in volcanic regions (Hill, 1977) and a similar model proposed by Sibson (1996) have often been used to interpret MS cloud growth (Evans et al., 2005; Häring et al., 2008). In these models, the conjugate fractures (which can be regarded as optimally oriented faults) and extensional fractures comprise the fracture mesh. The first faults that slip during fluid injection, are typically optimally oriented with respect to the in situ stress field. These faults strike approximately 30° off the direction of σ_1. Microseismic events often occur on both optimally oriented conjugate faults if they both exist. Consequently, the MS cloud grows in the direction of σ_1 from a macroscopic perspective, as presented in Fehler et al. (1987), Fehler (1989) and Häring et al. (2008). Meanwhile, the faults parallel to σ_1 can also undergo shear slip after pore pressure increases sufficiently. The normal stress on these faults is σ_3 so they are expected to have the highest permeability according to the theory between permeability and effective normal stress (e.g., Miller, 2015; Rice, 1993; Willis-Richards et al., 1996). Such a fault would accommodate significant fluid flow once injected fluid reached it, regardless of the occurrence of shear slip. Non-optimally oriented faults (especially conjugate forms) also contribute to the extension of the MS cloud in the direction of σ_1 with the increase of pore pressure, although they also contribute to expanding the width of the MS cloud due to their components that are not aligned with the σ_1 direction. Thus, the MS cloud should extend in the direction of σ_1 if there are existing fracture distributions consistent with the in situ stress.

This is similar to the well-known insight of fracture propagation in hydraulic fracturing cases. Fracture initiation occurs when fluid pressure exceeds σ_3 by the tensile strength. Nucleated fractures extend in the direction of σ_1 (Hubbert & Willis, 1972); thus, the MS cloud also extends in the orientation of σ_1. The MS cloud deviates from the orientation of σ_1 once the extending fractures meet the natural fracture systems, or it thickens if branching occurs. Thus, MS cloud growth in the case of hydraulic fracturing is attributed to much simpler flow and failure phenomena than it would be in the case of hydraulic stimulation into fracture networks.

In the EGS projects of Basel, Switzerland, and Soultz, France, both of which are located within the Rhine Graben, the shape of the MS cloud was consistent with the σ_1 orientation (Evans et al., 2005; Häring et al., 2008; Mukuhira et al., 2013; Soma et al., 2007). However, this empirical relationship cannot always explain the shape of other observed MS clouds. As a counterexample, the hot fracture rock project in the Cooper Basin, Australia, had a different feature, in that the observed MS cloud was mainly delineated by one or a few subhorizontal fractures

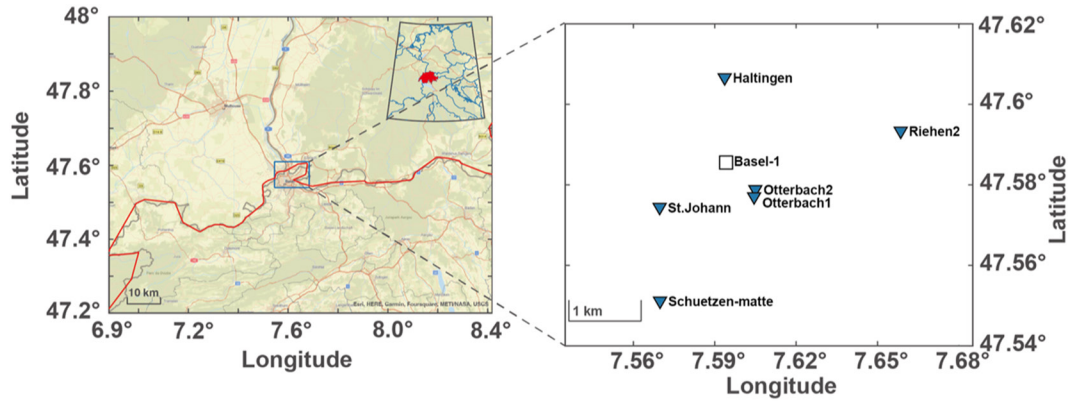

Figure 1. Location of Basel, Switzerland (left) and the microseismic monitoring network of the Basel EGS project in Basel City (right; blue inverted triangles). The square represents the location of the injection well, Basel-1.

(Baisch et al., 2006); the planar MS cloud did not grow in the σ_1 orientation. Thus, the MS cloud of the Cooper Basin was heavily controlled by the dominant horizontal existing fractures as opposed to in situ stress. Another counterexample is the recent interpretation on the Fenton Hill Hot Dry Rock (HDR) test site in the United States, in which the MS cloud did not extend to the σ_1 orientation (Norbeck et al., 2018). Tezuka and Niitsuma (2000) discussed the shape of the MS cloud of the Hijiori HDR test site, Japan, which had a biased distribution based on the existing fractures. These examples indicate that MS cloud growth behavior is very complicated and is not yet fully understood, especially in three-dimensional (3D) situations.

Recent studies have shown that microseismic analysis can provide a very detailed map of the fracture system using relocation techniques (Asanuma et al., 2008; Kraft & Deichmann, 2014). However, the phenomena associated with reservoir creation within an existing fracture system are too complicated in terms of relocation uncertainty and the potential effects of aseismic fracture. Therefore, we take a macroscopic approach to evaluating reservoir creation processes in terms of the MS cloud growth shape by attempting to clarify its relationships to in situ stress, existing fracture distribution, and pore pressure. We utilize well-recorded microseismicity, in situ stress measurements, and existing fracture data from the EGS project in Basel, Switzerland as a case study. Then, we discuss whether the insights from the analysis may explain the MS cloud growth behavior of other fields considering in situ stress and existing fracture conditions.

2. Data and Methods

2.1. Field Description

We studied microseismic activity observed at the EGS reservoir hydraulic stimulation project in Basel, Switzerland, in 2006. The EGS project aimed to create an artificial geothermal reservoir to provide hot water for electricity generation and heating as a co-generation system. Basel is located at the southern end of the Upper Rhine Graben, characterized by having the highest geothermal potential in Europe (Baria et al., 1999; Charléty et al., 2007) (Figure 1). The injection well, Basel-1, was drilled in the urban part of the city to a depth of approximately 5,000 m from the surface. A granitic basement was encountered below the upper sedimentary section, which has a thickness up to 2,500 m. The casing shoe was installed to approximately 4,630 m, and the remaining 400 m of the open-hole section was subjected to stimulation. Hydraulic stimulation was conducted for approximately 5 days, beginning on 2 December 2006. The maximum flow rate was 3300 L/min, accompanied by a wellhead pressure reaching 29.6 MPa (Häring et al., 2008). Injected water penetrated the formation via the cataclastic zone at the top of the open-hole section of the injection well, which was located at approximately 4,670 m depth (Dyer et al., 2008; Häring et al., 2008). Hydraulic stimulation successfully caused numerous microseismic events. Seismic activity increased with the flow rate and wellhead pressure, and the MS cloud extended during the hydraulic stimulation process. On the fifth day of hydraulic stimulation, microseismic activity had risen to an undesirable level (Häring et al., 2008). Despite a reduction in flow rate, seismic activity continued and several felt events, including the largest event (Mw 3.41), occurred during the shut-in phase (Häring et al., 2008; Mukuhira et al., 2013). Microseismic activity continued even after half a year following the termination of stimulation

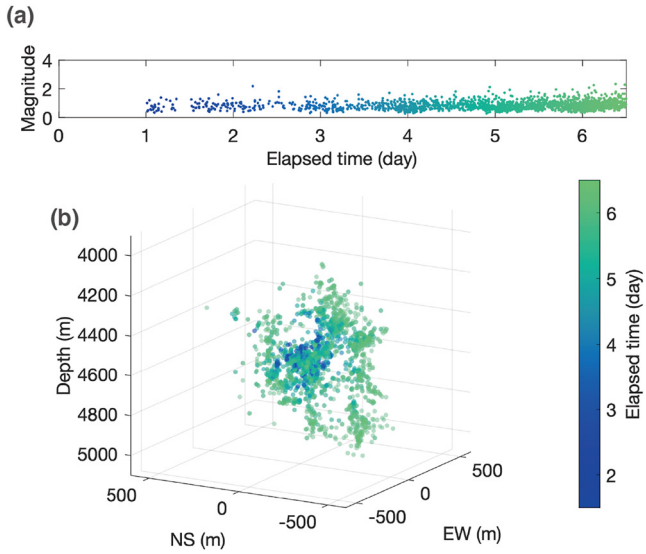

Figure 2. (a) Magnitude-time (M-t) plot for the stimulation period. The color in the M-t plot indicates the elapsed time since the start of the stimulation for the microseismicity. The end of the plot is the time of shut-in. (b) Three-dimensional figure showing the hypocenter distribution of microseismic events with timing indicated by color.

(Mukuhira et al., 2013), and seismic activity continued until at least 2018 (Herrmann et al., 2019).

2.2. Microseismic Data

The primary operator of the EGS project, Geothermal Explorers Ltd. (GEL), installed a microseismic network consisting of six downhole seismometers and one sensor in the injection well (Figure 1) (see Data Availability Statement for data access). The deepest seismometer, Otterbach 2, was installed at the top of the granite section, and other seismometers were installed in the sediment. One temporary geophone was deployed in Basel-1 at 4,720 m from the surface to capture the event signals at the very early stages of stimulation. The data from these events were used to calibrate the velocity model, assuming that those events occurred within 100 m from the injection point. Following this, a single layer (i.e., between sediment and granite) velocity model was used for hypocenter determination by GEL (Dyer et al., 2008). Until the tenth day from the onset of stimulation, the microseismic monitoring system detected around 13,500 triggers of potential events, whereby ∼3,100 events were located.

In this study, we used the hypocenter locations determined by Asanuma et al. (2008). Asanuma et al. (2007, 2008) provided an independent analysis on the same microseismic data set used in Dyer et al. (2010). They manually picked the P- and S-wave arrivals and then determined the hypocenters, which were almost identical to those determined by Dyer et al. (2008). They also applied multiplet analysis (Moriya et al., 2002) to detect the relative time of arrival for P- and S-waves. Approximately 70% of microseismic events could be grouped into 100 clusters. Relocated clusters using a double difference method (Waldhauser & Ellsworth, 2000) delineated several sub-fractures in the reservoir (Asanuma et al., 2008). The spatial error in the absolute hypocenter locations was approximately 40 m, and the error in the relative hypocenter locations was less than 10 m in horizontal direction. The error ellipsoids were entirely sub-vertical, with the longest axes dimension being at least 100 m, which was a bit worse than the lateral resolution (Asanuma et al., 2007). The MS cloud had a sub-vertical geometry striking in the NNW-SSE direction macroscopically.

In addition to the earthquake catalog used (Mukuhira et al., 2021) here and that from Dyer et al. (2008), other research groups have generated earthquake catalogs. Deichmann and Giardini (2009) and Kraft and Deichmann (2014) used the catalog based on regional surface networks. Kraft and Deichmann (2014) precisely analyzed microseismic data from the downhole network and conducted relocation using a different frequency band and clustering algorithm from those of Asanuma et al. (2007). However, the overall shape of the MS cloud from Kraft and Deichmann (2014) is similar to that used in this study; thus, it was determined that discrepancies between the catalogs would not be a critical problem for the purpose of this study. Recently, Herrmann et al. (2019) detected more microseismic events occurring as recently as in 2018, using a matched filter technique at a single station, and providing detection time and magnitude.

Figure 2 shows a 3D overview of the MS cloud for the stimulation period (until the shut-in). Microseismic activity began near the injection well and then expanded outward. Seismic activity near the injection well continued with the increase in flow rate. During the shut-in and bleeding-off phase (∼5 days after the shut-in), pore pressure re-distribution occurred. This caused very active microseismic activity in the periphery of the previously stimulated region (see details in Mukuhira, Dinske, et al. (2017)). However, this study only focused on the stimulation phase since the interaction between pore pressure migration and the occurrence of microseismicity was clear in the stimulation phase.

2.3. In Situ Stress and Natural Fracture Data

The orientation and magnitude of the in situ stress in the study area were previously investigated using borehole logging data (Valley & Evans, 2009, 2015, 2019). Based on borehole breakout and drilling-induced tensile

fracture data (Valley & Evans, 2009), the orientation of the maximum horizontal stress was estimated to be N144°E ± 14°. Recently, Valley and Evans (2019) revised the in situ stress magnitude based on consideration of borehole breakout, drilling-induced tensile fractures, and several other failure criteria, following their previous estimates (Valley & Evans, 2015). The linear depth trends of stress magnitude proposed by Valley and Evans (2019) were $Sv = 24.9z$, $S_{hmin} = 7z + 42$, and $S_{Hmax} = 5z + 90$, with the unit of stress being MPa and z being the depth in km from the surface. This small gradient in S_{Hmax} led to the stress state transitioning at 4,200 m from a strike-slip regime above to a normal faulting regime below. The estimated in situ stress model was consistent with the observed mix of strike-slip and normal fault-type focal mechanisms of larger induced seismic events (Deichmann & Giardini, 2009). We use this in situ stress model, assuming a laterally homogeneous stress state in the reservoir region, for comparison with MS cloud growth and interpretation.

In a related study, several natural fractures were detected from borehole image data obtained with a Schlumberger Ultrasonic Borehole Imager (UBI), and those natural fractures were extensively analyzed (Ziegler, et al., 2015; Ziegler & Evans, 2020). At depth, the reservoir was dominated by NNW-SSE striking fractures, roughly parallel to the S_{Hmax} direction and thus consistent with the current in situ stress regime; however, a wide variety of natural fractures in the granite section were also present, including those striking NE-SW nearly perpendicular to the orientation of S_{Hmax} (Ziegler et al., 2015). Some of those fractures were identified in association with the fractures delineated within the microseismic cluster (Ziegler & Evans, 2020).

2.4. Principal Component Analysis (PCA)

We applied PCA to the hypocenter location data of microseismicity in time steps to quantitatively and statistically characterize the growth of MS cloud shape. PCA is a data analysis technique to characterize data distribution and can be applicable for the decomposition of high dimensional data to lower dimensions, and it has recently been used in unsupervised machine learning analysis (e.g., Shu et al., 2018). In general, PCA detects the basis along which the variance of the data distribution is maximized. In practice, principal components are computed by eigen decomposition of the data variance-covariance matrix, which, in this study, consisted of the hypocenter coordinates, and the principal components are considered eigenvectors of the covariance matrix. The variance of the microseismic hypocenter tends to be at its maximum along with the first principal component, meaning that the MS cloud's axis of largest extension is in the direction of the first principal component. PCA has also been used to evaluate the shape and orientation of seismic clusters and to detect the structures from hypocenters (Michelini & Bolt, 1986; Moriya et al., 2003; Mukuhira et al., 2013; Vidale & Shearer, 2006; Xue et al., 2018).

We applied PCA to microseismic hypocenters consisting of the MS cloud and then extracted the three principal components to characterize the MS cloud shape (for detailed procedure, please see appendix), assuming that the MS cloud grows from the point of injection source, which is the case for EGS hydraulic stimulation. We define the data matrix $\mathbf{M}$, which consists of hypocenter location of n microseismic events, in an analysis window defined with time or space.

$$\mathbf{M} = \begin{pmatrix} x_1 & \cdots & x_n \\ y_1 & \cdots & y_n \\ z_1 & \cdots & z_n \end{pmatrix} \quad (1)$$

Note that we did not fix the centroid point of the hypocenters in PCA. The lengths of each component were computed from the eigen values, and then we used the square root of variances (standard deviation) that were increased by a factor of three. Effectively, three orthogonal principal components can model the MS cloud as an ellipsoid defined by the components' directions and lengths. The resulting ellipsoid should include 99% of microseismic events. Note that we did not intend to model the MS cloud as an ellipsoid as MS cloud shape is not always ellipsoidal.

We also examine the effect of the uncertainty in each hypocenter location by applying Uncertainty-Aware Principal Component Analysis (Ua-PCA), which estimates the principal component vector and length considering the uncertainty of each datum (Görtler et al., 2020). Here, we use the uncertainty in absolute location determined with Joint Hypocenter Location Method (Pujol, 2000). Of course, the uncertainty in absolute location is bigger than that in relative location. Therefore, our approach considers the effect of uncertainty in a conservative way.

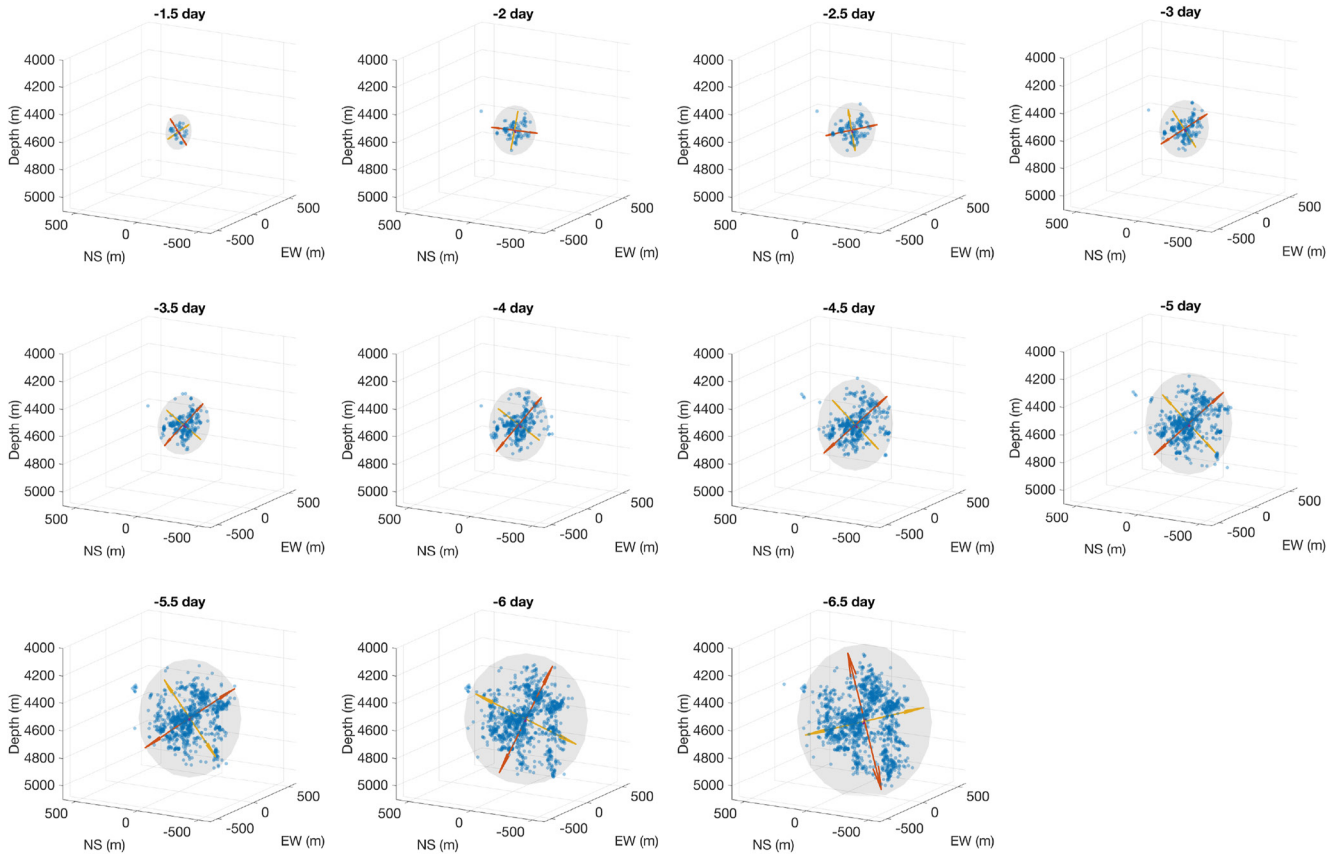

Figure 3. Snapshots of the 3D hypocenter distribution of microseismic events taken every 0.5 days from the start of the stimulation. The red, yellow, and purple arrows correspond to the first, second, and third principal components that describe representative ellipsoids for MS clouds at each time. Note that purple arrows are mostly hidden by the markers for hypocenters, a result of the third PCA being very small.

The error ellipsoid shape for each event in the reservoir was similar and the longer axes were oriented in the vertical direction (Asanuma et al., 2007). We project error ellipsoids to our hypocenter coordinate system and assume that they represent the error distribution along each axis direction. The errors projected along EW, NW, and Depth axes are shown in Figure S1 in Supporting Information S1. Ua-PCA results are shown accompanied with PCA results in the following analysis.

3. Analysis

3.1. Three-Dimensional MS Cloud Growth

First, we computed the three principal components of the MS cloud at 0.5-day intervals. The MS cloud of each time step included all microseismic events occurring since the beginning of injection. Figure 3 shows the 3D microseismic distribution for each time step and the ellipsoids defined with three principal components. The distribution of microseismic events changed with time; however, the ellipsoids shown in Figure 3 did not change significantly. The first PCA component (depicted by red) was more horizontal in the early few days and commenced dipping around 45° from the horizontal on the third day. The first and second principal components sometimes switched by 180° according to the local and temporal progress of the MS cloud. The 180° transition of each PCA component posed no issue in terms of its relationship with the MS cloud growth and in situ stress due to the symmetry of the in situ stress. The first and second principal components switched directions at 4.5 and 5 days. At the end of stimulation (6.5 days), the orientation of the first and second principal components showed different behavior compared to that prior to that time step during stimulation as follows. The first PCA component dipped in the NW direction at first, but then became more vertical at 6.5 days, and the second PCA component stayed close to vertical throughout, which is more evident in Figures 4a and 4b. It should be noted that the wellhead pressure increased gradually until the sixth day and then decreased due to flow rate reduction from 6 to ~6.5 days.

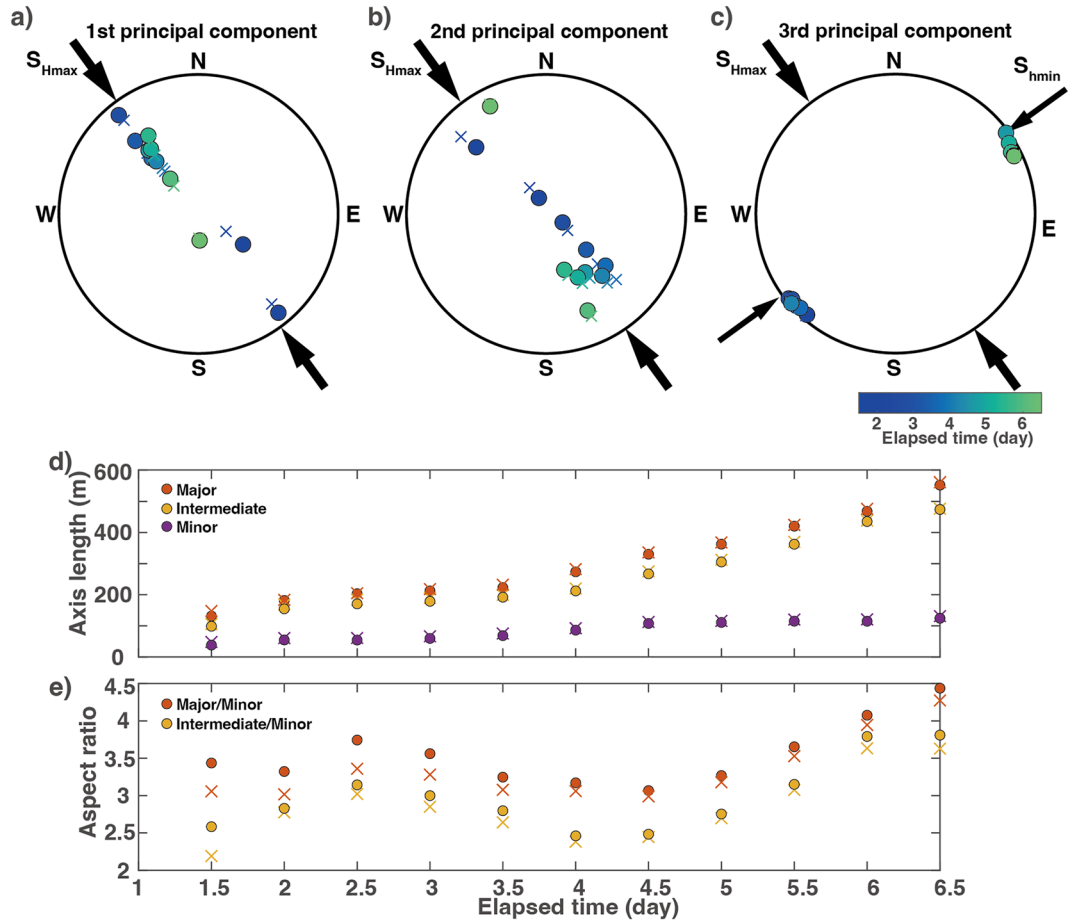

Figure 4. Time series change of first, second, and third principal component vectors: (a) major; (b) intermediate; and (c) minor axes orientation for representative ellipsoids in the lower hemisphere projections. Circles are the results of PCA and crosses are the results of Ua-PCA. The presented principal component vectors are the same as those shown in Figure 3; (d) time series for change of principal component length (major, intermediate, and minor axes lengths); and (e) the aspect ratio between the first to third principal component lengths (red) and second to third principal component lengths (yellow). Crosses correspond to the results from Ua-PCA.

The orientation of the computed principal components is summarized in the lower hemisphere plot in Figures 4a–4c, which represents the time series change of the MS cloud growth orientation. We observed that in the orientation of the third principal component, the minor orientation of MS cloud growth was constant and almost identical to the minimum horizontal stress, S_{hmin} direction. In contrast, the first and second principal components changed in the plane perpendicular to the orientation of S_{hmin}. Figure 4d shows the time series changes of each principal component length, while Figure 4e shows the aspect ratio for the first and second principal components relative to the third one. The first and second principal components had nearly similar values throughout the stimulation period shown in Figure 4d. In contrast, the third principal component grew to 120 m at most; this was around one-fourth the length of the first and intermediate principal components. The aspect ratios between components varied together between 2.5 and 4. The PCA results for each incremental time step is shown in Figure S2 in Supporting Information S1; the results are almost the same as those shown here. The uncertainty in hypocentral location did not influence the PCA results significantly, but some deviations can be seen in Figures 4a and 4b, where vertical location errors were taken into account.

3.2. Depth Dependence of MS Cloud Growth

We investigated the MS cloud shape further within different depth intervals. We applied PCA to microseismic events within 100-m thick depth sections, with no overlap between them. We computed only two principal components, ignoring the depths of each microseismic event. Microseismic events that originated along the same

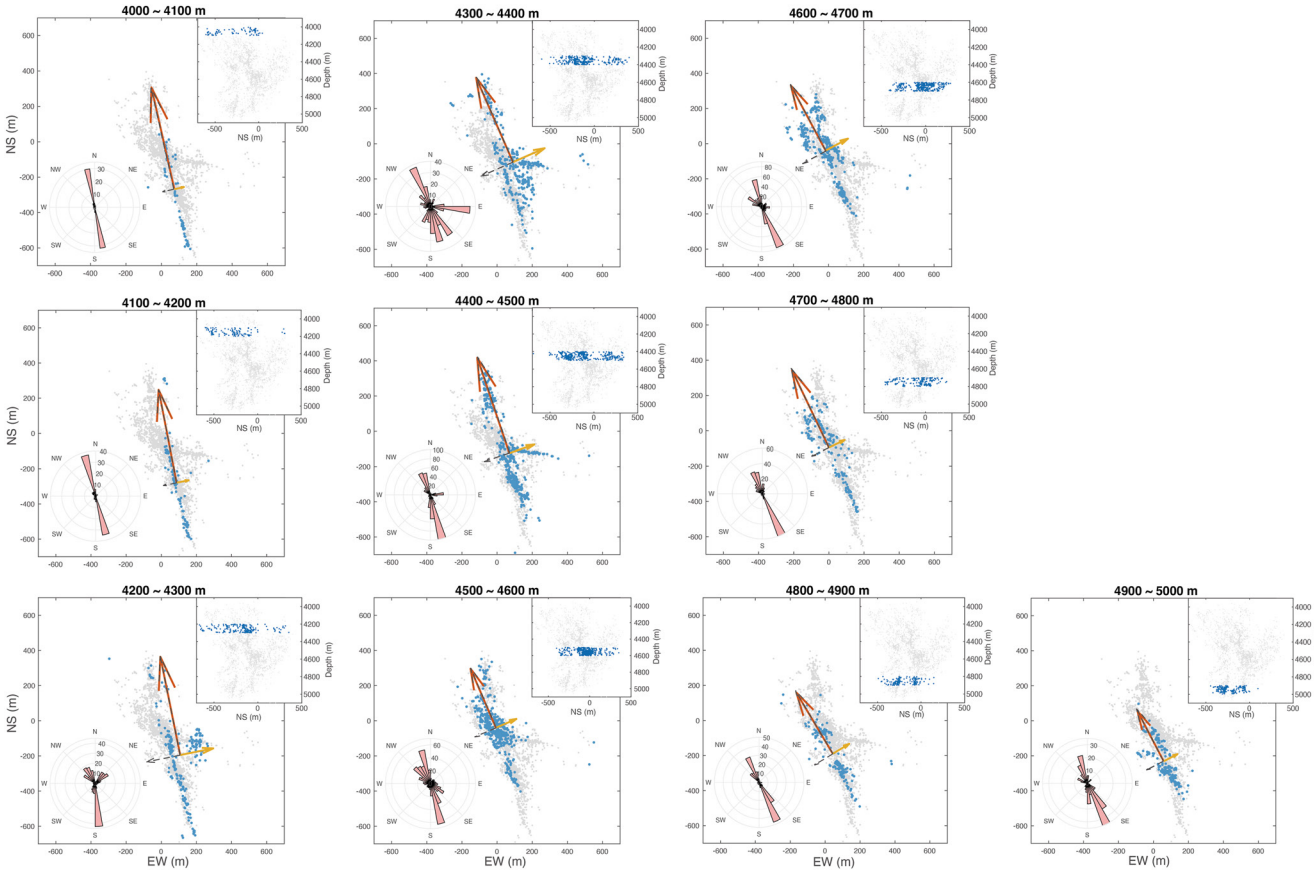

Figure 5. Hypocenter distribution of events for different 100 m depth sections in horizontal view. The blue dots are the event hypocenters within the target depth. The results of the two-dimensional (2D) PCA are shown with two arrows (red and orange). Ua-PCA results are also shown with two gray broken line arrows. The larger of the two Ua-PCA components is overplotted on that of standard PCA and is thus difficult to see. The upper right inset of each panel is a N-S cross-section highlighting the events within target depth. The gray dots denote all microseismic events. The left lower inset represents the rose diagram for geometrical orientations from the centroid point to each event.

vertical fractures are divided into several depth sections. In addition to the principal components, the geometric relationship between the centroid point of the selected MS cloud to each hypocenter is summarized as a rose diagram, shown for each panel of Figure 5.

We observed a linear MS cloud shape in the shallower part of the reservoir (4,000–4,200 m), where there is almost no variation in the orientation of seismicity within this depth interval. Below 4,200 m, the MS cloud thickens owing to events occurring along multiple fractures. These features resulted in the extension of the second principal component and an elliptical shape for the entire MS cloud. This tendency was especially observed in the MS cloud at the depths 4,200–4,700 m. In the 4,300–4,400 m depth section, the MS cloud was very diffuse, and the rose diagram shows very different shapes compared to those at shallower depths. Seismic activity was observed in branch fractures striking E-W at 4,400–4,500 m. At this depth, the northern MS cloud appeared independent of the main and southern parts of the MS cloud. In the next depth section of 4,500–4,600 m, the densest seismic activity moved slightly north, as demonstrated by the centroid point of the MS cloud. In the deeper sections of the reservoir, the MS cloud could be divided into northern and southern parts according to its seismic and aseismic regions.

Despite the depth-dependent features of microseismic activity and associated MS cloud shape, the macroscopic trend of the MS shape was maintained as the MS cloud extended in an orientation almost identical to S_{Hmax}. Figure 6a summarizes the azimuths of the first principal component with depth and shows that the azimuth of the first principal component slightly rotated from N-S to NW-SE with an increase in depth. We visualized the existing fractures delineated by multiplet analysis (clustering analysis) at each depth in Figure S3 in Supporting Information S1. The aspect ratios of the MS cloud at each depth section were between 2 and 4, with the exception

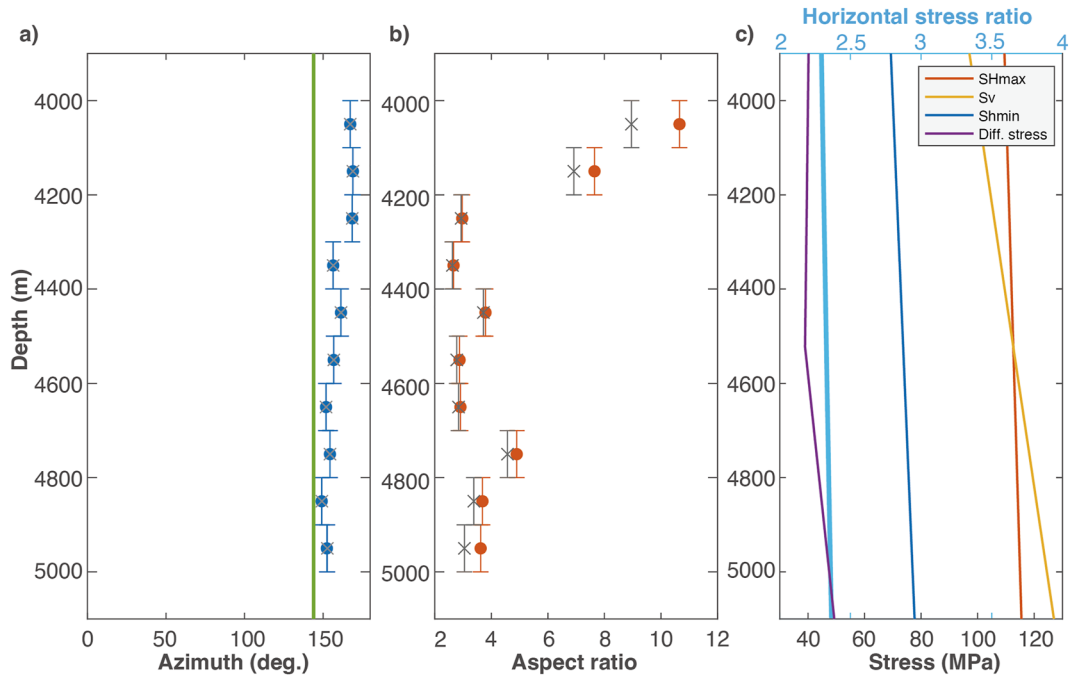

Figure 6. (a) Orientation of the first principal component as a function of depth. Each vertical bar indicates the depth of the analyzed section, while the vertical green line shows the orientation of S_{Hmax}; (b) aspect ratio between the lengths of the first and second principal components; and (c) the stress profile and horizontal stress ratio $(S_{Hmax} - p_{hyd})/(S_{hmin} - p_{hyd})$. Ua-PCA results are shown with gray crosses in (a) and (b).

of those at depths at 4,700–4,800 m, as shown in Figure 6. At shallower depths, the aspect ratios exceeded 6; these exceptionally high aspect ratios reflect the vertically planar shape of the MS cloud at shallower depths. The results from Ua-PCA results provided slightly lower aspect ratio but they did not make a big difference in observation. It should be noted that the majority of the events above 4,200 m occurred following the shut-in operation.

Because we investigated the MS cloud shape in different depth sections, we estimated the horizontal stress ratio, defined as $(S_{Hmax} - p_{hyd})/(S_{hmin} - p_{hyd})$, for each depth (Figure 6c), where p_{hyd} is hydrostatic pore pressure. The horizontal stress ratio in the reservoir depth was approximately 2.3. The horizontal stress ratio was a bit smaller than the aspect ratio of the MS cloud, although it was fairly consistent with the aspect ratio of the MS cloud growth except for the two shallow sections.

3.3. Injection Depth MS Cloud Growth

During injection, the injected pore pressure migrates from the feed point in the well through the formation (Zoback, 2007). The pore pressure decays with distance from the injection point based on the permeabilities of existing fractures comprising the flow path, their connectivity, the injection pressure and so on. Thus, pore pressure migration is a complicated and nonlinear phenomenon. However, from our previous study (Mukuhira, Moriya, et al., 2017), we can reasonably assume that either the pore pressure in the vicinity of the injection point was as high as that at the well bottom, or the pore pressure decay was relatively small in the near-well field. Therefore, we can expect that the MS cloud shape near the injection point was linear or simple during the initial stage of stimulation, as only the well-oriented fractures are likely to experience shear failure. Later, the more non-optimally oriented existing faults may host shear slip as the pore pressure increases, making the MS cloud more spherical in shape. Based on this concept as a working hypothesis, we further investigated the time series change of the MS cloud shape at the injection depth.

We focused on MS cloud shape consisting of the events occurring between 4,500 and 4,700 m, which included the feed point (4,681 m) of the cataclastic zone (Häring et al., 2008). The microseismic activity started from this depth at the start of the stimulation (Figure 7, ~1.5 day panel). We focused on events located NS (North to South) > −200 m as we observed that the southern part of the MS cloud was divided by an aseismic zone and was

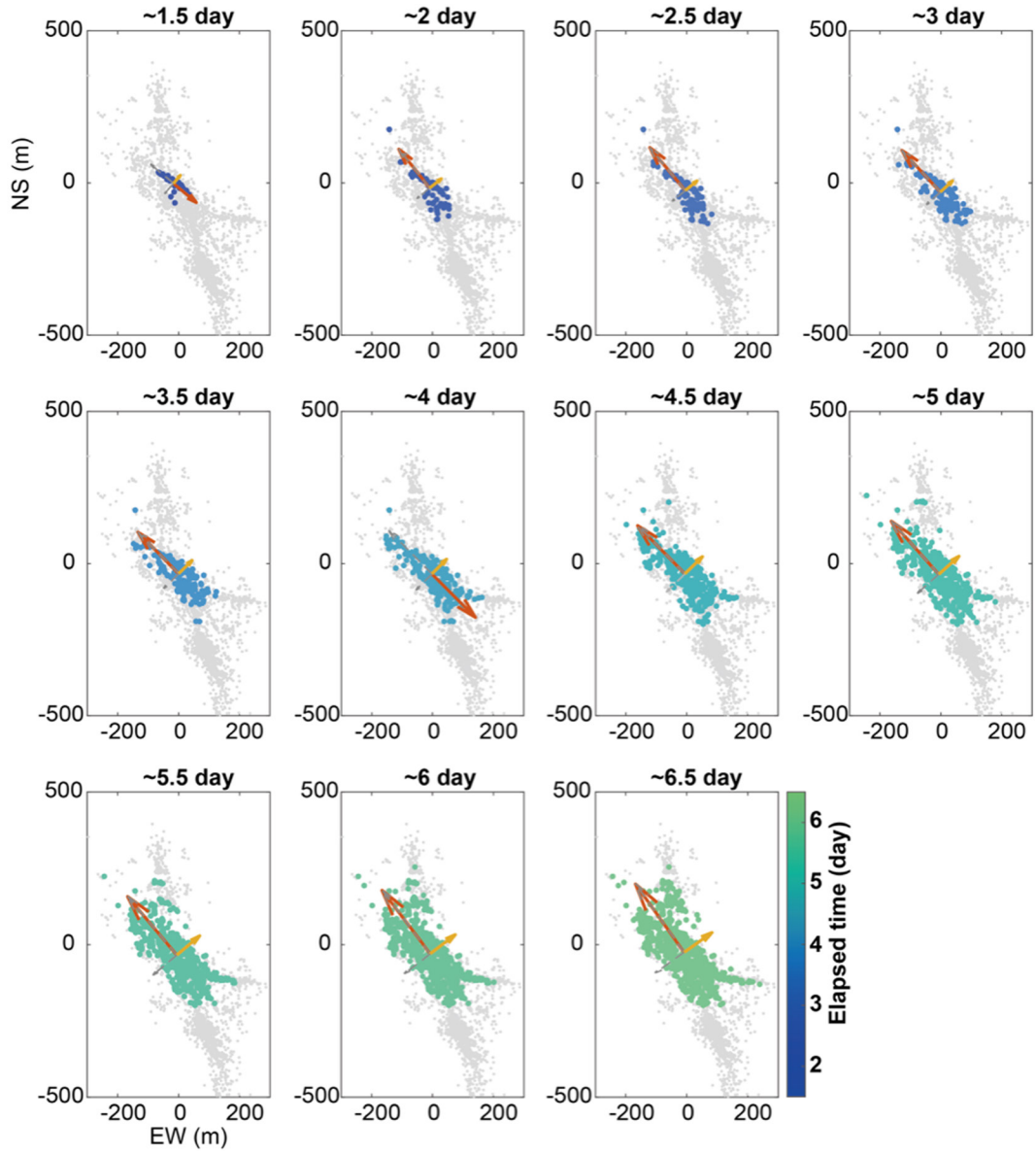

Figure 7. Time series evolution of microseismic events within the injection depth range of 4,500–4,700 m. Colored dots represent the events within the analysis depth and time window. Gray dots represent all hypocenters to show the shape of entire MS cloud. The 2D PCA results are depicted with two arrows; red: first component, yellow: second component. The 2D Ua-PCA results are also shown with two gray broken line arrows, although they are nearly identical to the standard PCA results. Dashed lines may be obscured by standard PCA results.

not directly connected to the injection zone as we discussed in 3.2 (Figure 5). We applied 2D PCA to a time series of MS cloud growth at every 0.5 days (Figure 7). The MS cloud had been droplet-shaped, linearly extending to the NW and forming an elliptical or circular shape near the injection point at 3.5 days of the stimulation. After 3.5 days, the MS cloud became thicker with time, and its shape became more elliptical. The incremental time analysis result is shown in Figure S4 in Supporting Information S1.

The relative geometry from the MS cloud centroid point is summarized in Figure 8a in the same manner as Figure 5. The rose diagram shows the orientation range of the MS cloud shape as it became wider over time (according to pore pressure increase). The rose diagram shape varies somewhat, suggesting that more events occurred in the northern direction. The time series change in the first and second principal components and their lengths are summarized in Figure 8b (standard PCA) and c (Ua-PCA). The orientation of the first principal

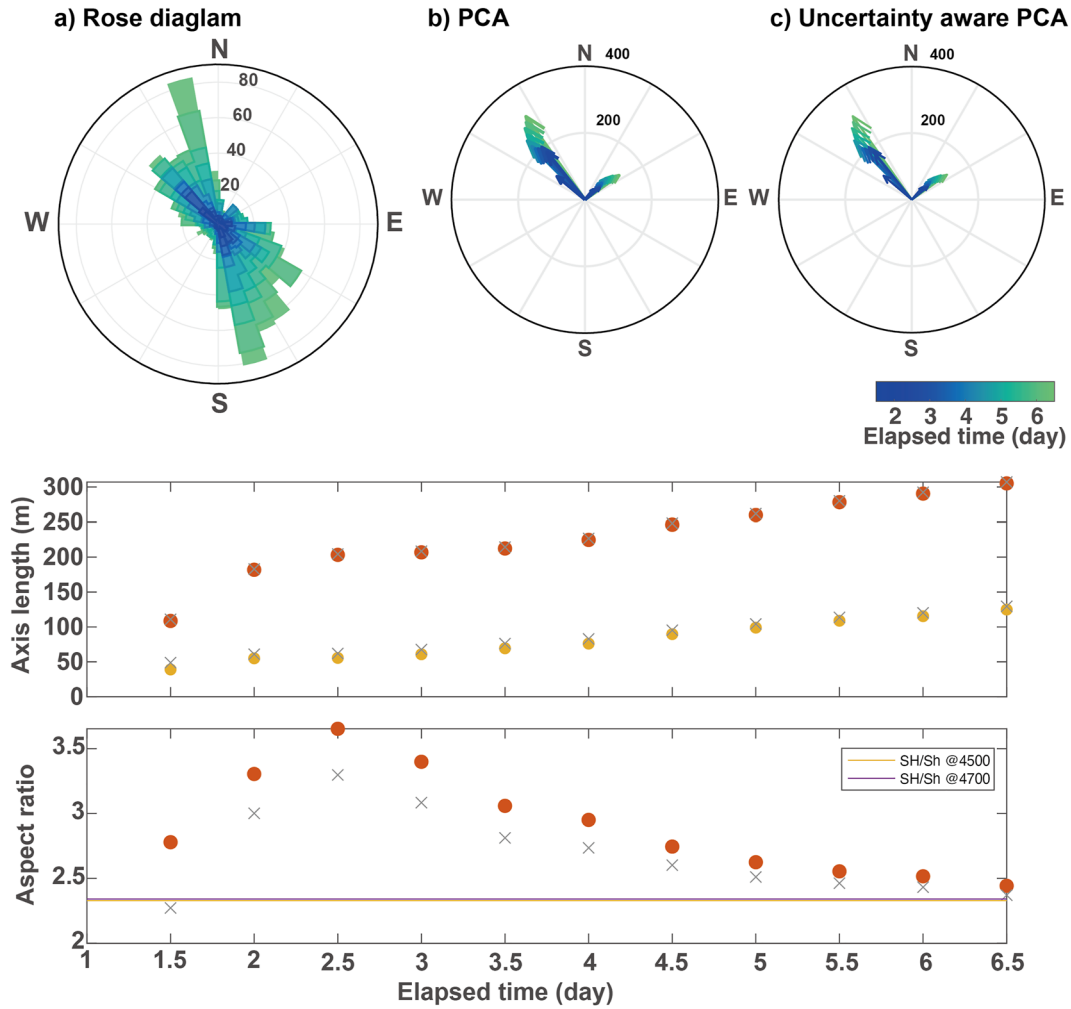

Figure 8. (a) Rose diagram of geometrical orientations from the centroid point of the MS cloud, with the color of the rose diagram corresponding to the analysis time; (b) time series change of orientation and length of the first and second principal components, again with the color corresponding to the analysis time; (c); Ua-PCA results in same format as (b); (d) length of first and second principal components as a function of time; (e) aspect ratio of first and second principal components as a function of time compared with the horizontal stress ratios at 4,500 and 4,700 m. Ua-PCA results are shown with gray crosses in (d) and (e).

component was more or less stable during stimulation. Therefore, the macroscopic MS cloud growth orientation was relatively preserved despite the change in the MS cloud shape. The aspect ratio increased gradually, reflecting a more linear MS cloud shape during the early stage of the stimulation. After 2.5 days, as we forecasted and observed in Figure 7, the aspect ratio of the MS cloud shape decreased, representing that the MS cloud became thicker and ellipsoidal in shape. Consequently, the aspect ratio decreased from 3.5 to 2.5. Note that the effective horizontal stress ratio at this depth was approximately 2.34.

The contribution to the whole MS cloud shape from each existing fracture is delineated with the microseismic clusters in supplementary Figure S5 in Supporting Information S1; the interaction among each existing fracture was difficult to see due to complexity.

3.4. Cross-Sectional MS Cloud Growth

We observed the cross-sectional MS cloud growth along the orientation of N144°E (N36°W), which is the same orientation as that of S_{Hmax}, and to correlate with in situ stress, we projected events into a vertical plane striking in the direction N36°W. This choice is reasonable based on the PCA results presented in Section 3.1. Figure 9

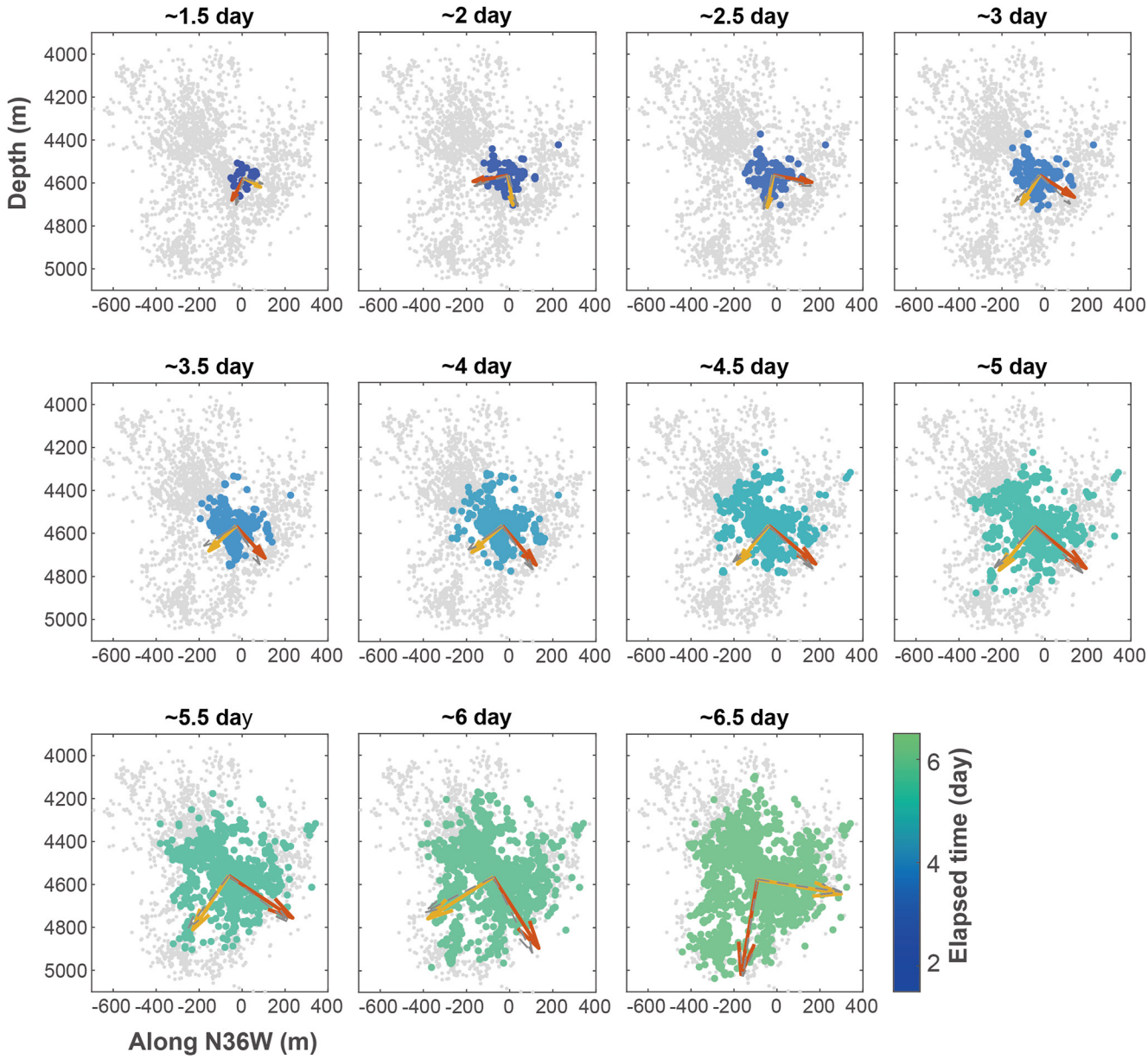

Figure 9. Time series evolution of microseismic events for the first 6.5 days of the stimulation projected onto a vertical plane trending the N36°W. Events that occurred within ±200 m from the intersection of the plane with the injection point were plotted and analyzed. The 2D PCA results are depicted with two arrows; red: first component, yellow: second component. The Ua-PCA results are depicted with two gray broken line arrows, which may be obscured by arrows for standard PCA results.

shows the time series evolutions of the MS cloud along the N36°W cross-section. For this analysis, we selected events that occurred within ±200 m from the base line along N36°W passing through the injection point (Figure S6 in Supporting Information S1). The incremental time series analysis is shown in Figure S7 in Supporting Information S1, and the multiplet analysis results are shown in Figure S8 in Supporting Information S1.

Until up to the third day, one of the principal components was nearly vertical (inclination < -80), and then its orientation changed dynamically. After the third day, one of the components started dipping. The orientation of the first and second principal components was quite stable between about 3.5 and 6.5 days and their length relationship was also nearly constant. The principal components showed different behavior at 6.5 days, in that the first principal component was oriented nearly vertically. These observations are basically the same as those of the 3D observations presented in Section 3.1. We visually confirmed that the MS cloud grew symmetrically, and that the MS cloud shape was more or less circular (Figure 9). The aspect ratio was between 1 and 1.3, and

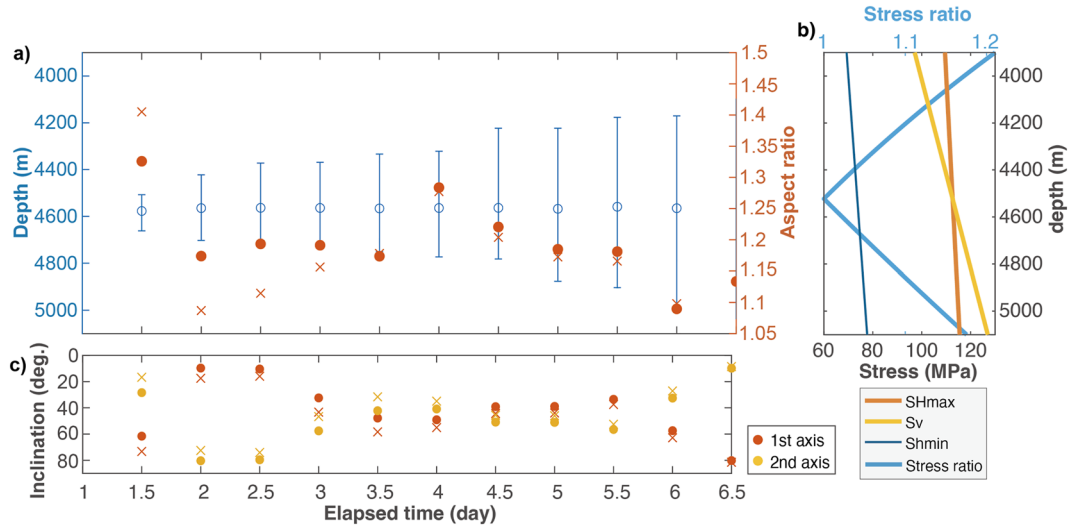

Figure 10. Correlation between MS cloud shape and in situ stress. (a) Circles correspond to the centroid depth of the MS cloud, and the error bar corresponds to the upper and lower limits of the MS cloud. Red dots show the aspect ratio of the first and second principal components of the MS cloud. Red crosses correspond the aspect ratio from Ua-PCA. (b) Stress profile and ratio of the vertical and maximum horizontal stresses. (c) Inclination of the first and second principal components. Crosses show the results from Ua-PCA.

was more stable than in the cases of horizontal depth slice analysis (Figure 10a). The ratio between S_{Hmax} and Sv was 1–1.15 in the target depth section (4,200–5,000 m), showing very good agreement with the MS cloud growth aspect ratio, even though the stress transition from the strike-slip regime to the normal fault regime occurred at around 4,500 m (Figure 10b).

4. Discussion

4.1. MS Cloud Growth Controlled by In Situ Stress

We have analyzed the following topics of the growth of the MS cloud at Basel, Switzerland ausing PCA: (a) 3D time series MS cloud, (b) depth sectional MS cloud, (c) time series of injection depth MS cloud, and (d) MS cloud in the plane of largest and intermediate principal stress. We find that the MS cloud shape was mainly controlled by in situ stress from the macroscopic perspective and that the MS cloud shape can be scaled with the in situ stress ratio.

4.1.1. Orientation of MS Cloud

The minor principal component was constantly oriented in the S_{hmin} direction, regardless of the scale change of the MS cloud over time (Figures 4 and 8). This observation suggests that MS cloud growth behavior in this field is a scale- and time-independent process, and that this process has macroscopic continuity throughout the reservoir. This observation also indicates the homogeneity of in situ stress within the reservoir.

The MS cloud extension did not always occur in the direction of σ_1 in a simple manner. Instead, it occurred in the plane perpendicular to the direction of σ_3. The orientation of the first and second principal components varied and sometimes flipped (Figure 4). These phenomena may be attributed to the competition of the maximum and intermediate principal stress magnitudes and the accompanying pore pressure distribution depending on the depth in the reservoir. Therefore, knowing the influence of the intermediate stress may improve understanding of MS cloud extension. From 2D horizontal MS cloud growth observations, the MS cloud extension orientation was more or less constant and consistent with the orientation of S_{Hmax} for different depths and time (Figures 6 and 8) despite the influence of various existing faults in each depth section and the time-dependent pore pressure distribution.

Previously, the MS clouds were considered to extend in the general direction of σ_1, based on a mesh-like fracture system (Hill, 1977; Sibson, 1996). Although this is partially in agreement with our observations, our observations

show that the MS cloud around Basel-1 did not always extend in the direction of σ_1. Sibson (1996) discussed that the permeability is preferably developed in the direction of the intermediate principal stress in his fracture mesh model. This interpretation is also partially in agreement with our observations, as MS cloud extends in the direction of σ_2. The MS cloud aspect ratio from depth sectional analysis in Figure 6 shows that the aspect ratios in the normal fault stress regime (below 4,500 m) of the MS cloud seem to be slightly larger than those in the strike-slip stress regime (4,200–4,500 m), which is consistent with Sibson's (1996) discussion. However, the fracture systems at Basel and elsewhere are much more complicated than the conceptual model. Consequently, all principal component directions are nearly parallel to the directions of principal stresses. The largest principal component was sub-vertical, which is consistent with the maximum principal direction in the deeper part of the reservoir.

4.1.2. Scaling of MS Cloud Shape

We evaluated the MS cloud shape by comparing the aspect ratios estimated from each principal component and the in situ stress ratio. The 3D MS cloud aspect ratios that we observed are similar to the ratios of the principal stresses (Figure 4d). This was also confirmed in the 2D MS cloud shape cross-section analysis, where we observed that the MS cloud aspect ratio was nearly identical to the stress ratio between S_{Hmax} and Sv (Figure 10).

The 2D MS cloud aspect ratios at different depths should reflect the pore pressure distribution. In the reservoir depth section (4,200–5,000 m), the horizontal stress ratio was nearly constant. However, the MS cloud shape ratio tended to be larger than the horizontal stress ratio. Meanwhile, the MS cloud shape at shallower depths was strongly linear in plane view, posing a higher aspect ratio (Figure 6b). The microseismic events at shallower depths were induced after the shut-in (Mukuhira, Dinske, et al., 2017). A tiny perturbation of pore pressure triggered these events, such that the delineated MS cloud showed the optimally oriented fractures. Thus, the shape of the MS cloud is also influenced by pore pressure migration. The same tendency was also observed in the 2D MS cloud shape observations near the injection depth. The MS cloud shape was more linear at the early stage of stimulation as the pore pressure remained low, and optimally oriented faults experienced shear failure. Then, the MS cloud shape became more elliptical with time, that is, the pore pressure increased because the non-optimally-oriented fault could fail. Figure 8e shows a clear tendency for the aspect ratio of the MS cloud to decrease with time, that is, with increasing pore pressure. It can be said that the pore pressure perturbation or existing fracture affects the MS cloud shape locally.

We did not explore the local interactions in detail as it was nearly impossible to link them to physical processes associated with microseismic activity and in situ stress (e.g., multiplet cluster analyses in Figures S3 or S7 in Supporting Information S1), nor would this be very informative for our purpose due to its complexity.

4.1.3. MS Cloud Growth and Fracture Permeability

We now discuss the observed correlation between MS cloud geometry and in situ stress ratio based on the insights of fracture permeability and geomechanics because pore pressure is also controlled by in situ stress. Rice (1993) proposed the following model for the stress-dependent permeability along a fracture: $k = k_0\exp(-\sigma_n/\sigma')$ where k is the permeability, k_0 is the permeability at no loading, σ_n is the effective normal stress, and σ' is a constant that determines the decay rate of the permeability. Another model considering shear dilation was proposed by Willis-Richards et al. (1996) based on the cubic law, where flow rate is a function of the cube of fracture aperture a and permeability k is expressed with the fracture aperture a: $k = a^2/12$, where $a = a_0/(1 + 9\sigma_n/\sigma'') + a_s$, a_0 is the fracture aperture at no loading, σ'' is the effective normal stress to cause 90% closure of aperture, and a_s is the change in aperture due to shear slip. Thus, permeability is influenced by shear dilation to some extent. From these theories, the permeability of each fracture is a function of its geometry relative to the in situ stress.

According to the borehole measurements, critically stressed fractures (well-oriented fractures) have higher permeability because of relatively lower normal stress and possible shear dilation in the past (Barton et al., 1995; Ito & Zoback, 2000). This is not entirely the same as the permeability prediction as a function of normal stress (Rice, 1992), but can potentially be explained by the other form of permeability prediction by Willis-Richards et al. (1996), although evaluation of past shear dilation is very difficult. We computed the effective normal stress for arbitrary faults and permeability at the injection depth of 4,600 m based on the in situ stress model. Permeability is computed using the equation by Rice (1992), where we assumed $k_0 = 4 \times 10^{-16}$ m^2 and $\alpha = 10^{-1}$ following Miller (2015). Note that this permeability is for one independent fracture and we assume that fracture permeability is purely mechanically dependent. Here, the effect of shear dilation is not considered; therefore, the

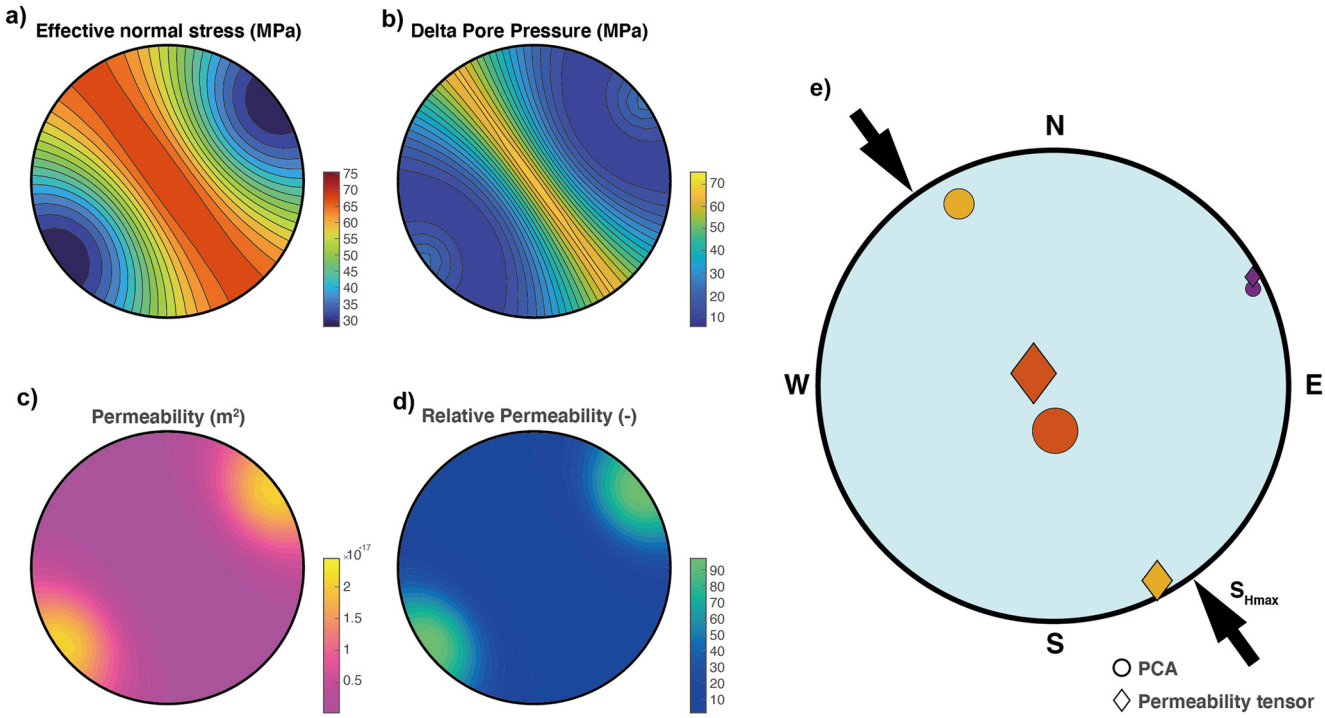

Figure 11. Distribution of (a) effective normal stress, (b) delta pore pressure for shear slip, (c) predicted permeability, and (d) normalized permeability (permeability in (c) is divided by the minimum permeability) to the poles of arbitrary fractures, based on the in situ stress model at 4,600 m. (e) Comparison between PCA results of MS cloud growth (circles) and bulk permeability (diffusivity) tensors (diamonds). Red: major, yellow: intermediate, and purple: minor principal component or tensor.

most permeable fractures are considered to be those perpendicular to the σ_3 direction since they have minimum effective normal stress (Figures 11a and 11c). We also computed critical pore pressure from the Coulomb failure criterion with friction coefficient 0.6 to show the distribution of well-oriented fractures. The minimum critical pore pressure position corresponds to the poles of well-oriented fractures. The permeability of the fracture perpendicular to the σ_3 orientation is higher than that of well-oriented fracture by a factor of 2.74 at the injection depth of 4,600 m (Figure 10c and Figure S9 in Supporting Information S1) if we can ignore past shear dilation.

We observed that the MS cloud extension to the direction of S_{Hmax} in the horizontal dimension exceeded the prediction from the in situ (horizontal) stress ratio. This observation might be interpreted with permeability differences between the well-oriented fractures and fractures perpendicular to the S_{hmin} as the flow path. While the MS cloud can extend somewhat along well-oriented fractures, pore pressure can extend more easily along the fracture perpendicular to S_{hmin} regardless of the shear slip. Another possible explanation is low permeability in the S_{hmin} direction. In this field, various natural fractures were identified using borehole logging analysis (Ziegler et al., 2015). Some of the existing fractures had strikes in the direction of S_{hmin} and nearly zero dip, which means they are perpendicular to S_{Hmax}. According to the fracture permeability evaluation, the fracture with the lowest permeability, which is perpendicular to σ_1, had a permeability nearly two orders of magnitude lower than that with the highest permeability (Figure 11d). Hence, we can consider that fractures perpendicular to σ_1 are practically impermeable even though they do exist. Therefore, the MS cloud growth in the σ_3 direction is attributed to the well-oriented fractures and other fractures that slipped, rather than fractures perpendicular to σ_1.

4.2. MS Cloud Growth and Permeability Tensor

We empirically determined the possible scaling relationship between the MS cloud shape and in situ stress; however, the physical relationship between them could not be established. Therefore, we pose the question: can MS cloud scaling with in situ stress be explained well with some physical process? To partially address this new and challenging question, we introduce the concept of permeability tensor. Microseismic events are triggered by pore pressure increase, which is controlled by pore pressure migration. Therefore, pore pressure migration behavior should be governed by the bulk permeability of the reservoir, which should be anisotropic. Bulk permeability

can be considered as the aggregation of fracture permeabilities of each existing fracture in the system. The fracture permeability is a function of effective normal stress. Thus, we estimate the bulk permeability tensor at the time of stimulation for the reservoir. Note that the natural bulk permeability tensor was altered by shear dilations associated with fluid injection, and we consider the apparent bulk permeability tensor as the permeability tensor which is achieved by hydraulic stimulation.

To estimate bulk permeability, we used the method proposed by Shapiro et al. (1997, 1999). In this method, a diffusivity tensor was inverted from spatio-temporal microseismic distribution on the assumption that microseismic activity was controlled by pore pressure diffusion process. We inverted for the 3D diffusivity tensor along with three orthogonal principal bases. Then, a diffusivity tensor was converted to a permeability tensor. We obtained a diffusivity tensor of $\boldsymbol{D} = (0.48 \times 10^{-1}, 0.31 \times 10^{-1}, 0.48 \times 10^{-2})$ [m^2/s] and permeability tensor as $\boldsymbol{K} = (5.43 \times 10^{-17}, 3.48 \times 10^{-17}, 5.41 \times 10^{-18})$ [m^2]. Note that these tensors are represented by their principal components. The orientation of the principal axes of the permeability tensor is compared with the PCA result at the end of stimulation (Figure 11e). Directions of the estimated permeability tensor showed a very good match with the orientation of the principal components of our PCA analysis. Furthermore, the magnitude relations were also consistent with the PCA results. The largest and intermediate permeabilities were quite close (at least in the same order of 10^{-17}), and they are 1 order of magnitude higher than the smallest permeability. A significant difference does not exist between largest and intermediate bulk permeability, showing the consistent similarity to the maximum and intermediate principal stresses (S_{Hmax} and Sv) of Basel, which are very close each other. From this analysis, we found that the bulk permeability tensor plays an important role in controlling the MS cloud shape, and they both qualitatively appear to be a function of in situ stress.

So far, we assumed purely hydro-mechanical process and we discuss the influence of other factors to cause failure, although the triggering process is not the topic we explore here. The static stress changes caused by shear slip of the events in this field were much smaller (1 MPa) than the pore pressure change (30 MPa) (Catalli et al., 2013). A poroelastic effect might be the major causal trigger in a much larger scale of injection (e.g., Barbour et al., 2017; Goebel & Brodsky, 2018), but a poroelastic stress change is much smaller (less than 0.5 MPa) than the direct pore pressure effect in small-scale EGS injections as studied by Segall and Lu (2015), Chang et al. (2020), and Lim et al. (2020). Therefore, we consider that the local stress changes due to static and poroelastic stress change are negligible. We assumed that such a small local stress change is not significant for our study of macroscopic MS cloud shape, as macroscopic background stress should control the macroscopic behavior of seismicity. Some recent studies (e.g., De Barros et al., 2021) investigated the migration of the seismic front influenced by the aseismic slip by numerical simulation with a single fault model. However, many of the EGS reservoirs consist of fracture networks, and such an influence by aseismic slip to the seismic front is hard to be considered.

There is no doubt that the spatio-temporal evolution of the permeability tensor is closely related to the MS cloud growth behavior in fractured systems, but it is strongly constrained by the preexisting fracture distribution. Thus, further observation and systematic numerical simulations may confirm their physical links.

4.3. Comparison With Other EGS Fields

Here we consider how the insights derived from this study may explain the MS cloud growth in other EGS fields. We selected eight cases of EGS and HDR projects and reviewed the MS cloud growth features by comparing the in situ stress information based on published literature. The reliability of microseismic and in situ stress information is highly site dependent, and the project year also impacts reliability based on the available technologies at the time. All available information related to MS cloud shape and in situ stress is summarized in Table 1. The details of each field are documented Text S1 in Supporting Information S1). Here we quickly review for each site the characteristics of the MS cloud shape, distribution of existing fractures (if available) and in situ stress.

The MS cloud of the Soultz-sous-Forêts EGS field (France), 1993, showed the most consistent characteristics to our field, likely owing to the Soultz field being part of the Rhine Graben and having the same tectonic setting as Basel. There were existing fractures whose orientations are consistent with in situ stress, and they were mainly stimulated (Baria et al., 1999; Evans, 2005; Moriya et al., 2002, 2003). Other EGS fields such as Desert Peak, United States (Davatzes & Hickman, 2009; Lutz et al., 2010; Zemach et al., 2013), Hijiori, Japan (Oikawa & Yamaguchi, 2000; Sasaki & Kaieda, 2002; Tezuka & Niitsuma, 2000), and Ogachi second, Japan (Hori et al., 1994; Kaieda et al., 1992, 2010) also showed consistent features in that their MS clouds extended

Journal of Geophysical Research: Solid Earth

10.1029/2023JB026839

Table 1
Summary of MS Cloud Growth Behavior and Consistency With In Situ Stress for EGS/HDF Fields; SS Indicates Strike-Slip Type, NF Indicates Normal Fault Type, and RF Indicates Reverse Fault Type

Field	Num. of MS event	Natural fracture	Stress regime	S_{Hmax} orientation	MS cloud orientation	Stress ratio	MS cloud dimension	Consistency with in situ stress	References
The MS cloud of the Soultz-sous-Forêts EGS field (France) at 1993	10,000 (located)	N-S vertical/Stress consistent	SS or NF	N170°E ± 15°	N25°W	1:1:0.5	1: 0.8: 0.3	Stress consistent	Baria et al. (1999); Evans, (2005); Moriya et al. (2003, 2002)
Cooper Basin, Australia, 2003	11,000 (located)	Subhorizontal	RF	N110°E	NNE-SSW	NA	1: 0.75: 0.1	Existing fracture dominant	Baisch et al. (2006); Reynolds et al. (2005)
Fenton hill, US, 1983		N30°W	SS or NF	N30°E	NNW-SSE	1:1:0.5	1:1:0.2	Existing fracture dominant	Fehler et al. (1987, 1989); Brown et al. (2012); Norbeck et al. (2018)
Desert Peak, US, 2010, 2011	303 (located) 2200 (triggered)	Normal fault: ESE and WNW	SS or NF	N24°E	NNE-SSW	1:1∼0.8: 0.6	1: 1: 0.2	Stress consistent	Zemach et al. (2013); Lutz et al. (2010); Davatzes and Hickman (2009)
Pohang, South Korea, 2017	519 (located)	NA	RF	N77°E	N214°E	1:0.5:0.4	1:0.5:0.2	Stress inconsistent	Korean Government Commission (2019); Ellsworth et al. (2019)
Helsinki, Finland, 2018	6,150 (located)	NW-SE	SS	N110°E	NW-SE	1:0.75:0.45	NA	Stress consistent	Kwiatek et al. (2019)
Hijiori, Japan, 1986	∼200 (located)	Various/stress consistent	NF	EW	Strike in the E-W, dipping in N	1:0.7:0.6	1:1:0.4	Stress consistent	Sasaki and Kaieda (2002); Tezuka and Niitsuma (2000); Oikawa and Yamaguchi (2000)
Ogachi, Japan, 1992	1554 (1st)	NE-SW or NNE-SSW/High dip	SS or NF	EW	N20°E (1st)	1:1:0.9	1:0.5:0.2 (1st)	Existing fracture dominant (1st)	Kaieda et al. (1992); Hori et al. (1994); Kaieda et al. (2010)
	1,000 (2nd) (located)	Highly developed in shallow part (1st)	SS or NF	EW	N100°E (2nd)	1:0.6:0.5	1:0.5:0.25 (2nd)	Stress consistent (2nd)	

along the orientation of σ_1. However, the MS cloud shapes did not always conform to the in situ stress ratio for some fields, such as Helsinki, Finland, which, in that case, was probably due to the non-point source injection caused by multi-stage stimulation and packer leak (Kwiatek et al., 2019). The Ogachi (Japan) field showed different MS cloud growth features in the first (existing fracture dominant) and second (stress consistent) stimulations (Hori et al., 1994; Kaieda et al., 1992, 2010). Another EGS field, Pohang (Korea), showed MS cloud extension behavior that was too difficult to interpret (Ellsworth et al., 2019; Korean Government Commission, 2019).

Other EGS fields, including Cooper Basin, Australia, and Fenton Hill, United States, exhibit findings opposite to those noted in our study. In both fields, the MS clouds did not extend in the direction of any in situ stress. These phenomena were attributed to the strong preference for existing fracture distributions. In Cooper Basin, there were almost all subhorizontal sets of existing fractures that led to a very thin MS cloud (Baisch et al., 2006), which likely explains the lack of correlation to in situ stress. At Fenton Hill, the dominant existing fracture sets were not consistent with the current in situ stress state, and the seismicity was largely controlled by the existing fracture sets, such that the MS cloud was offset from the maximum horizontal stress direction (Norbeck et al., 2018); however, the MS cloud shape ratio was consistent with the stress ratio.

Thus, we conclude that if there are sufficient variations in existing fractures in the fields, the MS cloud growth process is controlled by in situ stress, and the MS cloud shape can be predicted by the in situ stress ratio. However, in fields with strong existing fracture preferences with few variations, the distribution of existing fractures is likely to have a dominant role in determining the MS cloud shape. It is very challenging to predict the shape of the MS cloud in these cases. The existing fracture distribution information from borehole logging could be a key to determining the dominant parameter for MS cloud geometry, as well as the numerical modeling approach (e.g., Norbeck et al., 2018).

5. Summary

This study investigated how a microseismic (MS) cloud grows during hydraulic stimulation by applying PCA to the microseismic hypocenter distribution obtained at the Basel EGS hydraulic stimulation project. Through PCA, the orientation of MS cloud growth was derived quantitatively and macroscopically. The MS cloud behavior characterized by PCA was compared with in situ stress information, and their correlation was discussed and compared with those observed for other field cases.

We find that:

- The MS cloud growth did not always extend to the maximum principal stress direction but did extend in the plane perpendicular to the minimum principal stress direction. The intermediate principal stress is not negligible for the microseismic cloud generation process.
- The MS cloud shape ratios estimated using PCA in 2D (horizontal or cross-sectional), and 3D were consistent with in situ (effective) stress ratios. The MS cloud from different depth sections showed an aspect ratio similar to the effective horizontal stress ratio, although the MS cloud ratio was overestimated relative to the stress ratio. The cross-sectional MS cloud along the orientation of S_{Hmax} was circular, reflecting the very close stress magnitude of S_{Hmax} and S_v.
- The apparent permeability tensor estimated from microseismic hypocenter distribution data showed a good agreement with MS cloud growth in terms of orientation and magnitude relation. The MS cloud shape can be attributed to this permeability anisotropy, which should be a function of in situ stress.
- Insights from this study are applicable to the MS cloud growth features for different EGS/HDR fields, especially when existing fractures show large variations (stress consistent case). However, there are other cases where the strong preference for existing fractures may play a more dominant role in controlling MS cloud growth.

In this study, we heuristically found and concluded that MS cloud growth direction and shape are mainly controlled by in situ stress, particularly where existing fractures show great variability in orientation, such as in the case of the Basel EGS hydraulic stimulation project. This study advances the understanding of the reservoir creation process, especially in a macroscopic sense. A more complete understanding of the reservoir creation process could be developed by including the physical explanation of how MS cloud shape or bulk permeability can be related to the in situ stress. Further research on a systematic evaluation between the MS cloud shape and in situ stress on various existing fracture distribution conditions could be carried out with numerical simulation.

Finally, the findings of this study also emphasize the usefulness of reliable stress measurements to provide more meaningful information on the reservoir creation process.

Appendix A: Prinicipal Component Analysis on Earthquake Hypocenter

Suppose M is the 3 by n matrix consisted by earthquake locations in consideration.

$$\mathbf{M} = \begin{pmatrix} x_1 & \cdots & x_n \\ y_1 & \cdots & y_n \\ z_1 & \cdots & z_n \end{pmatrix} \tag{A1}$$

Based on **M**, we get correlation matrix **C** and then premultiply and postmultiply **D** to get the variance covariance matrix **Σ**.

$$\Sigma = \mathbf{DCD} \tag{A2}$$

where

$$\mathbf{D} = \begin{pmatrix} \sigma_x & 0 & 0 \\ 0 & \sigma_y & 0 \\ 0 & 0 & \sigma_z \end{pmatrix} \tag{A3}$$

Here, σ_n $(n = x, y, z)$ is the standard deviation on each basis.

Eigenvalue decomposition is performed on **Σ** to get the Eigen values **Λ** and corresponding Eigen vectors V, which are principal components and their vectors.

$$\Sigma = V \Lambda V^T \tag{A4}$$

where $\Lambda = \mathrm{diag}[\lambda_1,\lambda_2,\lambda_3]$, $V = [v_1,v_2,v_3]$.

Conflict of Interest

The authors declare no conflicts of interest relevant to this study.

Data Availability Statement

The microseismic catalog data containing the location, magnitude, and cluster information is uploaded to the MIT institutional repository via the following link: https://dspace.mit.edu/handle/1721.1/129552 (Mukuhira et al., 2021). The code used for Ua-PCA is available in open repository at https://doi.org/10.6084/m9.figshare.23666310.v1. In situ stress, loggig result and other data are available within the articles properly cited and referred to in the reference list.

Acknowledgments
We thank N. Watanabe, E. S. Cochran, S. Hecker, and G. W. Chongfor discussions and comments on the manuscript. We also thank M. O. Häring, Geo Explorers Ltd. and Geo-Energie Suisse AG for providing the microseismic wave data. We thank the editor R. Abercrombie and the associate editor for their constructive comments. Reviews by M. C. Fehler, and anonymous reviewer improved this manuscript significantly. This study was supported by an R&D project for super-critical geothermal field development supported by NEDO and JSPS KAKENHI Grant JP21H05201 in Grant-in-Aid for Transformative Research Areas (A) "Science of Slow-to-Fast Earthquakes". Part of the work was carried out under the Collaborative Research Project of the Institute of Fluid Science, Tohoku University. Any use of trade, firm, or product names is for descriptive purposes only and does not imply endorsement by the U.S. Government.

References

Asanuma, H., Kumano, Y., Hotta, A., Niitsuma, H., Schanz, U., & Häring, M. (2007). Analysis of microseismic events from a stimulation at Basel, Switzerland. *GRC Transactions*, *31*, 265–270.

Asanuma, H., Kumano, Y., Niitsuma, H., Schanz, U., & Häring, M. (2008). Interpretation of reservoir structure from super-resolution mapping of microseismic multiplets from stimulation at Basel, Switzerland in 2006. *GRC Transactions*, *32*, 65–70.

Baisch, S., Weidler, R., Vörös, R., Wyborn, D., & de Graaf, L. (2006). Induced seismicity during the stimulation of a geothermal HFR reservoir in the Cooper Basin, Australia. *Bulletin of the Seismological Society of America*, *96*(6), 2242–2256. https://doi.org/10.1785/0120050255

Barbour, A. J., Norbeck, J. H., & Rubinstein, J. L. (2017). The effects of varying injection rates in Osage County, Oklahoma, on the 2016 Mw 5.8 Pawnee earthquake. *Seismological Research Letters*, *88*(4), 1040–1053. https://doi.org/10.1785/0220170003

Baria, R., Baumgärtner, J., Gérard, A., Jung, R., & Garnish, J. (1999). European HDR Research Programme at Soultz-sous-Forets (France) 1987-1996. *Geothermics*, *28*(4–5), 655–669. https://doi.org/10.1016/S0375-6505(99)00036-X

Barton, C. A., Zoback, M. D., & Moos, D. (1995). Fluid flow along potentially active faults in crystalline rock. *Geology*, *23*(8), 683–686. https://doi.org/10.1130/0091-7613(1995)023<0683

Brown, D., Duchane, D., Heiken, G., & Hriscu, V. (2012). *Mining the Earth's heat: Hot dry rock geothermal energy*. Springer.

Catalli, F., Meier, M. A., & Wiemer, S. (2013). The role of Coulomb stress changes for injection-induced seismicity: The Basel enhanced geothermal system. *Geophysical Research Letters*, *40*(1), 72–77. https://doi.org/10.1029/2012gl054147

Chang, K. W., Yoon, H., Kim, Y. H., & Lee, M. Y. (2020). Operational and geological controls of coupled poroelastic stressing and pore-pressure accumulation along faults: Induced earthquakes in Pohang, South Korea. *Scientific Reports*, *10*, 1–12. https://doi.org/10.1038/s41598-020-58881-z

Charléty, J., Cuenot, N., Dorbath, L., Dorbath, C., Haessler, H., & Frogneux, M. (2007). Large earthquakes during hydraulic stimulations at the geothermal site of Soultz-sous-Forêts. *International Journal of Rock Mechanics and Mining Sciences*, *44*(8), 1091–1105. https://doi.org/10.1016/j.ijrmms.2007.06.003

Davatzes, N., & Hickman, H. (2009). Fracture, stress and fluid flow prior to stimulation of well 27-15, Desert Peak, Nevada, EGS project. In *Proceedings of the 34th Workshop on Geothermal Reservoir Engineering, Stanford, CA*.

De Barros, L., Wynants-Morel, N., Cappa, F., & Danré, P. (2021). Migration of fluid-induced seismicity reveals the seismogenic state of faults. *Journal of Geophysical Research: Solid Earth*, *126*(11), e2021JB022767. https://doi.org/10.1029/2021JB022767

Deichmann, N., & Giardini, D. (2009). Earthquakes induced by the stimulation of an enhanced geothermal system below Basel (Switzerland). *Seismological Research Letters*, *80*(5), 784–798. https://doi.org/10.1785/gssrl.80.5.784

Dyer, B. C., Schanz, U., Ladner, F., Häring, M. O., & Spillman, T. (2008). Microseismic imaging of a geothermal reservoir stimulation. *The Leading Edge*, *27*(7), 856–869. https://doi.org/10.1190/1.2954024

Dyer, B. C., Schanz, U., Spillmann, T., Ladner, F., & Häring, M. O. (2010). Application of microseismic multiplet analysis to the Basel geothermal reservoir stimulation events. *Geophysical Prospecting*, *58*(5), 791–807. https://doi.org/10.1111/j.1365-2478.2010.00902.x

Ellsworth, W. L. (2013). Injection-induced earthquakes. *Science*, *341*(6142), 1225942. https://doi.org/10.1126/science.1225942

Ellsworth, W. L., Giardini, D., Townend, J., Ge, S., & Shimamoto, T. (2019). Triggering of the Pohang, Korea, Earthquake (Mw 5.5) by enhanced geothermal system stimulation. *Seismological Research Letters*, *90*(5), 1844–1858. https://doi.org/10.1785/0220190102

Evans, K. F. (2005). Permeability creation and damage due to massive fluid injections into granite at 3.5 km at Soultz: 2. Critical stress and fracture strength. *Journal of Geophysical Research B: Solid Earth*, *110*(4), 1–14. https://doi.org/10.1029/2004JB003169

Evans, K. F., Moriya, H., Niitsuma, H., Jones, R. H., Phillips, W. S., Genter, A., et al. (2005). Microseismicity and permeability enhancement of hydrogeologic structures during massive fluid injections into granite at 3 km depth at the Soultz HDR site. *Geophysical Journal International*, *160*(1), 388–412. https://doi.org/10.1111/j.1365-246X.2004.02474.x

Evans, K. F., Zappone, A., Kraft, T., Deichmann, N., & Moia, F. (2012). A survey of the induced seismic responses to fluid injection in geothermal and CO_2 reservoirs in Europe. *Geothermics*, *41*, 30–54. https://doi.org/10.1016/j.geothermics.2011.08.002

Fehler, M., House, L., & Kaieda, H. (1987). Determining planes along which earthquakes occur: Method and application to earthquakes accompanying hydraulic fracturing. *Journal of Geophysical Research*, *92*(B9), 9407–9414. https://doi.org/10.1029/jb092ib09p09407

Fehler, M. C. (1989). Stress control of seismicity patterns observed during hydraulic fracturing experiments at the Fenton Hill hot dry rock geothermal energy site, New Mexico. *International Journal of Rock Mechanics and Mining Sciences and Geomechanics Abstracts*, *26*(3–4), 211–219. https://doi.org/10.1016/0148-9062(89)91971-2

Fehler, M. C., Jupe, A., & Asanuma, H. (2001). More than cloud: New techniques for characterizing reservoir structure using induced seismicity. *The Leading Edge*, *20*(3), 324–328. https://doi.org/10.1190/1.1438942

Gharti, H. N., Oye, V., Roth, M., & Kuhn, D. (2010). Automated microearthquake location using envelope stacking and robust global optimization. *Geophysics*, *75*(4), MA27–MA46. https://doi.org/10.1190/1.3432784

Goebel, T. H. W., & Brodsky, E. E. (2018). The spatial footprint of injection wells in a global compilation of induced earthquake sequences. *Science*, *80*(361), 899–904. https://doi.org/10.1126/science.aat5449

Görtler, J., Spinner, T., Streeb, D., Weiskopf, D., & Deussen, O. (2020). Uncertainty-aware principal component analysis. *IEEE Transactions on Visualization and Computer Graphics*, *26*(1), 822–831. https://doi.org/10.1109/TVCG.2019.2934812

Grigoli, F., Cesca, S., Krieger, L., Kriegerowski, M., Gammaldi, S., Horalek, J., et al. (2016). Automated microseismic event location using Master-Event Waveform Stacking. *Scientific Reports*, *6*(1), 25744. https://doi.org/10.1038/srep25744

Häring, M. O., Schanz, U., Ladner, F., & Dyer, B. C. (2008). Characterisation of the Basel 1 enhanced geothermal system. *Geothermics*, *37*(5), 469–495. https://doi.org/10.1016/j.geothermics.2008.06.002

Herrmann, M., Kraft, T., Tormann, T., Scarabello, L., & Wiemer, S. (2019). A consistent high-resolution catalog of induced seismicity in Basel based on matched filter detection and tailored post-processing. *Journal of Geophysical Research: Solid Earth*, *124*(8), 8449–8477. https://doi.org/10.1029/2019JB017468

Hill, D. P. (1977). A model for earthquake swarms. *Journal of Geophysical Research*, *82*(8), 1347–1352. https://doi.org/10.1029/JB082i008p01347

Hori, Y., Kitano, K., & Kaieda (1994). Outline of Ogachi project for HDR geothermal power in Japan. *GRC Transactions*, *18*, 439–443.

Hubbert, M. K., & Willis, D. G. (1972). Mechanics of hydraulic fracturing. *Transactions of Society of Petroleum Engineers of AIME*, *210*(01), 153–163. https://doi.org/10.2118/686-g

Ito, T., & Zoback, M. D. (2000). Fracture permeability and in situ stress to 7 km depth in the KTB Scientific Drillhole. *Geophysical Research Letters*, *27*(7), 1045–1048. https://doi.org/10.1029/1999gl011068

Kaieda, H., Ito, H., Kiho, K., Suzuki, K., Suenaga, H., & Shin, K. (1992). Ogachi project for HDR geothermal power in Japan first hydraulic fracturing results. *GRC Transactions*, *16*, 493–496.

Kaieda, H., Sasaki, S., & Wyborn, D. (2010). Comparison of characteristics of microearthquakes observed during hydraulic stimulation operations in Ogachi, Hijiori and Cooper Basin HDR projects. *Proceedings of the World Geothermal Congress*.

Kim, K.-H., Ree, J.-H., Kim, Y., Kim, S., Kang, S. Y., & Seo, W. (2018). Assessing whether the 2017 Mw 5.4 Pohang earthquake in South Korea was an induced event. *Science*, *360*(6392), 1007–1009. https://doi.org/10.1126/science.aat6081

Korean Government Commission. (2019). *Summary Report of the Korean Government Commission on Relations between the 2017 Pohang Earthquake and EGS Project*. Geological Society of Korea. https://doi.org/10.22719/KETEP-20183010111860

Kraft, T., & Deichmann, N. (2014). High-precision relocation and focal mechanism of the injection-induced seismicity at the Basel EGS. *Geothermics*, *52*, 59–73. https://doi.org/10.1016/j.geothermics.2014.05.014

Kwiatek, G., Saarno, T., Ader, T., Bluemle, F., Bohnhoff, M., Chendorain, M., et al. (2019). Controlling fluid-induced seismicity during a 6.1-km-deep geothermal stimulation in Finland. *Science Advances*, *5*(5), 1–12. https://doi.org/10.1126/sciadv.aav7224

Lim, H., Deng, K., Kim, Y., Ree, J., Song, T. A., & Kim, K. (2020). The 2017 Mw 5.5 Pohang Earthquake, South Korea, and poroelastic stress changes associated with fluid injection. *Journal of Geophysical Research: Solid Earth*, *125*(6), 1–18. https://doi.org/10.1029/2019jb019134

Lutz, S. J., Hickman, S., Davatzes, N., Zemach, E., Drakos, P., & Robertson-Tait, A. (2010). Rock mechanical testing and petrologic analysis in support of well stimulation activities at the Desert Peak geothermal field, Nevada. In *Proceedings of the 35th Workshop on Geothermal Reservoir Engineering, Stanford, CA*.

Majer, E. L., Baria, R., Stark, M., Oates, S., Bommer, J., Smith, B., & Asanuma, H. (2007). Induced seismicity associated with enhanced geothermal systems. *Geothermics*, *36*(3), 185–222. https://doi.org/10.1016/j.geothermics.2007.03.003

Michelini, A., & Bolt, B. A. (1986). Application of the principal parameters method to the 1983 Coalinga, California, aftershock sequence. *Bulletin of the Seismological Society of America*, *76*(2), 409–420. https://doi.org/10.1785/bssa0760020409

Miller, S. A. (2015). Modeling enhanced geothermal systems and the essential nature of large-scale changes in permeability at the onset of slip. *Geofluids*, *15*(1–2), 338–349. https://doi.org/10.1111/gfl.12108

Moriya, H., Nakazato, K., Niitsuma, H., & Baria, R. (2002). Detailed fracture system of the Soultz-sous-Forêts HDR field evaluated using microseismic multiplet analysis. *Pure and Applied Geophysics*, *159*(1–3), 517–541. https://doi.org/10.1007/PL00001263

Moriya, H., Niitsuma, H., & Baria, R. (2003). Multiplet-clustering analysis reveals structural details within the seismic. *Bulletin of the Seismological Society of America*, *93*(4), 1606–1620. https://doi.org/10.1785/0120020072

Mukuhira, Y., Asanuma, H., Niitsuma, H., & Häring, M. O. (2013). Characteristics of large-magnitude microseismic events recorded during and after stimulation of a geothermal reservoir at Basel, Switzerland. *Geothermics*, *45*, 1–17. https://doi.org/10.1016/j.geothermics.2012.07.005

Mukuhira, Y., Dinske, C., Asanuma, H., Ito, T., & Häring, M. O. (2017). Pore pressure behavior at the shut-in phase and causality of large induced seismicity at Basel, Switzerland. *Journal of Geophysical Research: Solid Earth*, *122*(1), 411–435. https://doi.org/10.1002/2016JB013338

Mukuhira, Y., Kumano, Y., Asanuma, H., Häring, M. O., & Fehler, M. (2021). *Catalog of locations of microseismic events accompanying the 2006-2007 fluid injection into the Basel Enhanced Geothermal System*. DSpace@MIT. Retrieved from https://hdl.handle.net/1721.1/129552

Mukuhira, Y., Moriya, H., Ito, T., Asanuma, H., & Häring, M. (2017). Pore pressure migration during hydraulic stimulation due to permeability enhancement by low-pressure subcritical fracture slip. *Geophysical Research Letters*, *44*(7), 3109–3118. https://doi.org/10.1002/2017gl072809

Norbeck, J. H., McClure, M. W., & Horne, R. N. (2018). Field observations at the Fenton Hill enhanced geothermal system test site support mixed-mechanism stimulation. *Geothermics*, *74*(March), 135–149. https://doi.org/10.1016/j.geothermics.2018.03.003

Oikawa, Y., & Yamaguchi, T. (2000). Stress measurement using rock core in an HDR field. *Proceedings of the World Geothermal Congress*, 3819–3822.

Pine, R. J., & Batchelor, A. S. (1984). Downward migration of shearing in jointed rock during hydraulic injections. *International Journal of Rock Mechanics and Mining Sciences*, *21*(5), 249–263. https://doi.org/10.1016/0148-9062(84)92681-0

Pujol, J. (2000). Joint event location: The JHD technique and applications to data from local seismic networks. In C. Thurber & N. Rabinowitz (Eds.), *Advances in seismic event location* (pp. 163–204). Kluwer Academic.

Reynolds, S. D., Mildren, S. D., Hillis, R. R., Meyer, J. J., & Flottmann, T. (2005). Maximum horizontal stress orientations in the Cooper Basin, Australia: Implications for plate-scale tectonics and local stress sources. *Geophysical Journal International*, *160*(1), 331–343. https://doi.org/10.1111/j.1365-246x.2004.02461.x

Rice, J. R. (1992). Chapter 20 Fault stress states, pore pressure distributions, and the weakness of the San Andreas fault. *International Geophysics*, *51*, 475–503. https://doi.org/10.1016/j.jvolgeores.2021.107317

Rice, J. R. (1993). Spatio-temporal complexity of slip on a fault. *Journal of Geophysical Research*, *98*(B6), 9885–9907. https://doi.org/10.1029/93JB00191

Roff, A., Phillips, W. S., & Brown, D. W. (1996). Joint structures determined by clustering microearthquakes using waveform amplitude ratios. *International Journal of Rock Mechanics and Mining Sciences and Geomechanics Abstracts*, *33*(6), 627–639. https://doi.org/10.1016/0148-9062(95)00077-1

Sasaki, S., & Kaieda, H. (2002). Determination of stress state from focal mechanisms of microseismic events induced during hydraulic injection at the Hijiori hot dry rock site. *Pure and Applied Geophysics*, *159*(1), 489–516. https://doi.org/10.1007/PL00001262

Segall, P., & Lu, S. (2015). Injection-induced seismicity: Poroelastic and earthquake nucleation effects. *Journal of Geophysical Research: Solid Earth*, *120*(7), 1–22. https://doi.org/10.1002/2015jb012060

Shapiro, S. A., Audigane, P., & Royer, J. J. (1999). Large-scale in situ permeability tensor of rocks from induced microseismicity. *Geophysical Journal International*, *137*(1), 207–213. https://doi.org/10.1046/j.1365-246X.1999.00781.x

Shapiro, S. A., Huenges, E., & Borm, G. (1997). Estimating the crust permeability from fluid-injection-induced seismic emission at the KTB site. *Geophysical Journal International*, *131*(2), 5–8. https://doi.org/10.1111/j.1365-246X.1997.tb01215.x

Shu, L., McIsaac, K., & Osinski, G. R. (2018). Learning spatial-spectral features for hyperspectral image classification. *IEEE Transactions on Geoscience and Remote Sensing*, *56*(9), 5138–5147. https://doi.org/10.1109/TGRS.2018.2809912

Sibson, R. H. (1996). Structural permeability of fluid-driven fault-fracture meshes. *Journal of Structural Geology*, *18*(8), 1031–1042. https://doi.org/10.1016/0191-8141(96)00032-6

Soma, N., Niitsuma, H., & Baria, R. (2007). Reflection imaging of deep reservoir structure based on three-dimensional hodogram analysis of multicomponent microseismic waveforms. *Journal of Geophysical Research*, *112*(11), 1–14. https://doi.org/10.1029/2005JB004216

Tezuka, K., & Niitsuma, H. (2000). Stress estimated using microseismic clusters and its relationship to the fracture system of the Hijiori hot dry rock reservoir. *Developments in Geotechnical Engineering*, *84*(C), 55–70. https://doi.org/10.1016/S0165-1250(00)80007-3

Valley, B., & Evans, K. F. (2009). Stress orientation to 5 km depth in the basement below Basel (Switzerland) from borehole failure analysis. *Swiss Journal of Geosciences*, *102*(3), 467–480. https://doi.org/10.1007/s00015-009-1335-z

Valley, B., & Evans, K. F. (2015). Estimation of the stress magnitudes in Basel enhanced geothermal system. *Proceedings World Geothermal Congress 2015*.

Valley, B., & Evans, K. F. (2019). Stress magnitudes in the Basel enhanced geothermal system. *International Journal of Rock Mechanics and Mining Sciences*, *118*, 1–20. https://doi.org/10.1016/j.ijrmms.2019.03.008

Vidale, J. E., & Shearer, P. M. (2006). A survey of 71 earthquake bursts across southern California: Exploring the role of pore fluid pressure fluctuations and aseismic slip as drivers. *Journal of Geophysical Research*, *111*(5), 1–12. https://doi.org/10.1029/2005JB004034

Waldhauser, F., & Ellsworth, W. L. (2000). A double-difference earthquake location algorithm: Method and application to the Northern Hayward Fault, California. *Bulletin of the Seismological Society of America*, *90*(6), 1353–1368. https://doi.org/10.1785/0120000006

Watanabe, N., Hirano, N., & Tsuchiya, N. (2008). Determination of aperture structure and fluid flow in a rock fracture by high-resolution numerical modeling on the basis of a flow-through experiment under confining pressure. *Water Resources Research*, *44*(6), 1–11. https://doi.org/10.1029/2006WR005411

Willis-Richards, J., Watanabe, K., & Takahashi, H. (1996). Progress toward a stochastic rock mechanics model of engineered geothermal systems. *Journal of Geophysical Research*, *101*(B8), 17481–17496. https://doi.org/10.1029/96jb00882

Xue, L., Bürgmann, R., Shelly, D. R., Johnson, C. W., & Taira, T. (2018). Kinematics of the 2015 San Ramon, California earthquake swarm: Implications for fault zone structure and driving mechanisms. *Earth and Planetary Science Letters*, *489*, 135–144. https://doi.org/10.1016/j.epsl.2018.02.018

Yeo, I. W., De Freitas, M. H., & Zimmerman, R. W. (1998). Effect of shear displacement on the aperture and permeability of a rock fracture. *International Journal of Rock Mechanics and Mining Sciences*, *35*(8), 1051–1070. https://doi.org/10.1016/S0148-9062(98)00165-X

Zemach, E., Drakos, P., Spielman, P., & Akerley, J. (2013). *Desert peak enhanced geothermal systems (EGS) project*. Draft Final Report. https://doi.org/10.2172/1373310

Ziegler, M., & Evans, K. F. (2020). Comparative study of Basel EGS reservoir faults inferred from analysis of microseismic cluster datasets with fracture zones obtained from well log analysis. *Journal of Structural Geology*, *130*, 103923. https://doi.org/10.1016/j.jsg.2019.103923

Ziegler, M., Valley, B., & Evans, K. F. (2015). Characterization of natural fractures and fracture sones of the Basel EGS reservoir inferred from geophysical logging of the Basel-1 well. *Proceedings World Geothermal Congress*.

Zoback, M. (2007). *Reservoir geomechanics*. Cambridge University Press.

References From the Supporting Information

Shin, K., Ito, H., & Oikawa, Y. (2000). Stress state at the Ogachi site. *Proc WGC*, 1749–1752.